

JGR Solid Earth

RESEARCH ARTICLE

10.1029/2023JB026704

Key Points:

- A matrix approach of passive seismology provides 3D imaging of the North Anatolian Fault, Turkey, over a depth range of 60 km
- Transmission matrix between the Earth surface and the underground is extracted by means of spatio-temporal correlations of seismic noise
- Time reversal of this transmission matrix enables a sharp compensation of the seismic velocity variations in the fault area

Supporting Information:

Supporting Information may be found in the online version of this article.

Correspondence to:

R. Touma and A. Aubry,
rita.touma@espci.fr;
alexandre.aubry@espci.fr

Citation:

Touma, R., Le Ber, A., Campillo, M., & Aubry, A. (2023). Imaging the crustal and upper mantle structure of the North Anatolian Fault: A transmission matrix framework for local adaptive focusing. *Journal of Geophysical Research: Solid Earth*, 128, e2023JB026704. <https://doi.org/10.1029/2023JB026704>

Received 10 MAR 2023

Accepted 19 OCT 2023

Author Contributions:

Conceptualization: Michel Campillo, Alexandre Aubry

Data curation: Michel Campillo

Funding acquisition: Michel Campillo, Alexandre Aubry

Investigation: Rita Touma

Methodology: Rita Touma, Arthur Le Ber, Alexandre Aubry

Project Administration: Michel Campillo, Alexandre Aubry

Resources: Michel Campillo

Supervision: Michel Campillo, Alexandre Aubry

© 2023. The Authors.

This is an open access article under the terms of the [Creative Commons Attribution License](https://creativecommons.org/licenses/by/4.0/), which permits use, distribution and reproduction in any medium, provided the original work is properly cited.

Imaging the Crustal and Upper Mantle Structure of the North Anatolian Fault: A Transmission Matrix Framework for Local Adaptive Focusing

Rita Touma^{1,2}, Arthur Le Ber¹ , Michel Campillo² , and Alexandre Aubry¹ 

¹Institut Langevin, ESPCI Paris, PSL University, CNRS, Paris, France, ²ISTerre, Université Grenoble Alpes, Maison des Géosciences, Grenoble, France

Abstract Imaging the structure of major fault zones is essential for our understanding of crustal deformations and their implications on seismic hazards. Investigating such complex regions presents several issues, including the variation of seismic velocity due to the diversity of geological units and the cumulative damage caused by earthquakes. Conventional migration techniques are in general strongly sensitive to the available velocity model. Here we apply a passive matrix imaging approach which is robust to the mismatch between this model and the real seismic velocity distribution. This method relies on the cross-correlation of ambient noise recorded by a geophone array. The resulting set of impulse responses form a reflection matrix that contains all the information about the subsurface. In particular, the reflected body waves can be leveraged to: (a) determine the transmission matrix between the Earth's surface and any point in the subsurface; (b) build a confocal image of the subsurface reflectivity with a transverse resolution only limited by diffraction. As a study case, we consider seismic noise (0.1–0.5 Hz) recorded by the Dense Array for Northern Anatolia that consists of 73 stations deployed for 18 months in the region of the 1999 Izmit earthquake. Passive matrix imaging reveals the scattering structure of the crust and upper mantle around the North Anatolian Fault zone over a depth range of 60 km. The results show that most of the scattering is associated with the Northern branch that passes throughout the crust and penetrates into the upper mantle.

Plain Language Summary Investigating the structure of major fault zones is important to understand the deformations of the Earth's crust and their potential impact on future earthquakes. However, the large variations of seismic velocity between different geological units drastically hampers the ability to image those areas. The North Anatolian Fault is no exception since it splits into two branches separating three major geological blocks in the region of the 1999 Izmit earthquake. To image the deep structure of this fault, seismic noise is here exploited to retrieve information on the body waves reflected by the underground heterogeneities. A three-dimensional map of the subsurface reflectivity is then built by applying methods originally developed in optical microscopy and ultrasound for deep imaging inside complex media. The inner structure of the Earth around the North Anatolian Fault is revealed. In particular, the Northern branch is shown to exhibit a strong damage pattern and a deep penetration inside the upper mantle.

1. Introduction

The North Anatolian Fault zone (NAFZ) is one of the major continental right-lateral strike slip faults, and forms a border between the Eurasian continent and the Anatolian block. With an extremely well developed surface expression, it is one of the most active faults in the Eastern Mediterranean region (Barka, 1992; Sengör, 1979). It is over 1,600 km long and extends from eastern Turkey in the east to Greece in the west and, historically, has been subject to many destructive earthquakes (Ambraseys & Finkel, 1995; Stein et al., 1997). The seismic activity of such large faults constitutes a continuous hazard/threat to the surrounding regions and big cities, especially Istanbul city located to the West of the fault.

Faults are well defined at the surface by the localized deformation and displacement delineating the fault traces, but their deep structure remains poorly understood (Vauchez et al., 2012). The understanding of such major fault systems and seismic hazard requires a characterization of the geometrical and seismic properties of the crust and upper mantle. A large number of geological and geophysical studies have discussed the complexity of fault zones and their relation with their deep roots (Stein et al., 1997). They are not only confined in the mid crust; indeed, models suggest that they penetrate deep into the crust and extend to the upper Mantle (Lyakhovskiy &

Validation: Rita Touma, Alexandre Aubry
Visualization: Rita Touma
Writing – original draft: Rita Touma, Michel Campillo, Alexandre Aubry

Ben-Zion, 2009). If so, faults develop into shear zones, corresponding to a volume of localized deformation accounting for the relative displacement of the tectonic blocks.

Seismic imaging techniques, especially reflection, refraction, and tomographic methods, constitute a very powerful tool to characterize fault zones and report the variation of the properties of the crust and the upper mantle. They rely on the study of wave propagation inside the Earth that is governed by the density and elastic properties of the rocks. To properly probe the medium, waves should be generated by a dense distribution of seismic sources. Conventional seismic exploration techniques use either earthquakes as seismic sources, or explosions and vibrators to generate seismic waves in regions with weak seismicity. Because of the limitations in the earthquake distribution and high cost of active methods, there is a need for alternative imaging approaches that would not rely on any coherent source. In the 2000's, the extraction of deterministic information about the Earth structure from ambient seismic noise revolutionized the field of seismology (see e.g., Campillo & Roux, 2014). It was shown that the cross-correlation of diffuse waves or ambient seismic noise recorded at two stations provides an estimate of the Green's function between those two stations (see e.g., Campillo & Paul, 2003). The reflection response of the medium is then retrieved and can be applied to build tomographic or structural images of the Earth. Because ambient noise is dominated by surface waves, their Green's function component can be easily extracted (Shapiro & Campillo, 2004). It has been demonstrated that, under energy equipartition, body wave reflections can also be retrieved from ambient seismic noise cross-correlations (Draganov et al., 2007; Poli, Campillo, Pedersen, & LAPNET Working Group, 2012; Poli, Pedersen, & Campillo, 2012). Body waves contain valuable information on the structure of the medium in depth and can be investigated to obtain high-resolution images of the crust and the mantle (Retailleau et al., 2020).

Faults are usually imaged indirectly through strong velocity contrasts in tomographic profiles (Zigone et al., 2019), or through the offset of geological layers observed in reflectivity images (Qian & Liu, 2020). However, tomographic images exhibit a relatively poor resolution, while reflection imaging methods are strongly sensitive to the available velocity model. Interestingly, a reflection matrix approach has been recently proposed to cope with these issues. Originally developed in acoustics (Lambert, Cobus, Couade, et al., 2020; Lambert, Cobus, Frappart, et al., 2020) and optics (Badon et al., 2020; Kang et al., 2017), this approach has been recently applied to passive seismology (Blondel et al., 2018; Touma et al., 2021). By considering high frequency seismic noise (10–20 Hz), high resolution images of complex areas, such as volcanoes (Giraudat et al., 2021) and fault zones (Touma et al., 2021), have been obtained over a few km depth. In this paper, we aim to characterize the crustal structure of the NAFZ at a much larger scale (until 60 km depth). To that aim, a lower frequency bandwidth (0.1–0.5 Hz) has been considered. At the corresponding wavelengths, the subsurface reflectivity can be considered as continuous rather than being seen as a discrete distribution of scatterers as in our previous works (Giraudat et al., 2021; Touma et al., 2021). As we will see, this continuous reflectivity can be exploited to enable a local and adapted auto-focus on each part of the subsurface image, thereby showing an important robustness to the inaccuracy of the initial wave velocity model.

Seismic matrix imaging is based on the passive measurement of the reflection matrix \mathbf{R} associated with a network of geophones. It contains the set of impulse responses between each pair of geophones extracted from cross-correlations of seismic noise. Based on the available velocity model, a focused reflection (FR) matrix is built by applying a redatuming process to \mathbf{R} (Blondel et al., 2018; Lambert, Cobus, Couade, et al., 2020). This matrix contains the impulse response between virtual sources and receivers synthesized inside the medium. In the following, matrix “input” and “output” will refer to virtual sources (downgoing waves) and receivers (upgoing waves), respectively. This FR matrix is powerful as it first provides an image of the subsurface reflectivity by considering its diagonal elements (i.e., when virtual source and receiver coincide); this is the *so-called* confocal image. Moreover, its off-diagonal elements allow a local quantification of aberrations in the vicinity of each virtual source. Those aberrations correspond to the imperfections of the image induced by the mismatch between the wave velocity model and the actual seismic velocity distribution in the subsurface. In contrast with previous works (Giraudat et al., 2021; Touma et al., 2021), a multi-layered wave velocity model is here considered rather than just an homogeneous model. This more sophisticated description of seismic wave propagation enables a better time-to-depth conversion in the confocal image and a better focusing process. Nevertheless, the FR matrix still highlights residual aberrations that result from the mismatch between the velocity model and the actual velocity distribution. The fluctuations of wave velocities actually induce phase distortions on the focused wave-fronts that result in a blurry image of the NAFZ subsurface.

To overcome these detrimental effects, the FR matrix can be first projected in a plane wave basis. By exploiting the angular input-output correlations of the reflection matrix, phase distortions of the incident and reflected wave-fronts can be identified and compensated. This is the principle of the CLASS algorithm (acronym for closed-loop accumulation of single scattering), originally developed in optical microscopy (Choi et al., 2018; Kang et al., 2017; Yoon et al., 2020). Applied for the first time to seismology in the present study, CLASS successfully compensates for spatially invariant aberrations and will be shown to clearly improve the confocal image of the NAFZ subsurface.

Nevertheless, high-order aberrations subsist and are addressed through the distortion matrix concept in a second step. Originally introduced in ultrasound imaging (Lambert, Cobus, Frappart, et al., 2020) and optical microscopy (Badon et al., 2020), this operator contains the phase distortions of the incident and reflected wave-fronts with respect to the propagation model. It was recently exploited in passive seismology in order to image the San Jacinto Fault zone scattering structure that exhibits a sparse distribution of scatterers (Touma et al., 2021). Here, we apply it in a new scattering regime since the NAFZ subsurface exhibits, in the frequency range under study, a continuous reflectivity distribution made of specular reflectors and randomly distributed heterogeneities. In this regime, a local time reversal analysis of the distortion matrix can be performed in order to retrieve the transmission matrix between the Earth's surface and any point of the subsurface (Lambert, Cobus, et al., 2022). This transmission matrix is a key tool since its phase conjugate provides the optimized focusing laws that need to be applied to the reflection matrix in order to retrieve a diffraction-limited image of the subsurface. While most conventional reflection imaging techniques are strongly sensitive to the available velocity model, the reflection matrix approach is robust with respect to its limitations. An approximate velocity distribution is actually sufficient since a time-reversal analysis of seismic data enables a local and adapted auto-focus on each part of the subsurface image.

To image the crustal structure of NAFZ, we use data from the Dense Array for Northern Anatolia (DANA, 2012) that was deployed over the western segment of the fault, in the latest rupture region during the 1999 Izmit ($M = 7.6$) and Düzce ($M = 7.2$) earthquakes (Akyuz et al., 2002; Barka et al., 2002). The dense array was installed temporarily between May 2012 and October 2013. It consists of 73 3-component broadband seismometers, 66 stations arranged along 11 east-west lines and 6 North-South lines forming a rectangular grid and covering an area of 35 km by 70 km with a nominal inter-station spacing of ~ 7 km (Figure 1a). Seven additional stations were deployed east of the rectangular array in a semi-circle shape. In this region, the fault splits into two major strands: the northern (NNAFZ) and southern (SNAFZ) strands (Figure 1b). The northern strand, where most of the continuous deformation occurs according to geodetic studies (Barka, 1992; Reilinger et al., 2006), has been subject to a series of major earthquakes in the last century, among them the 1999 Izmit Earthquake. On the contrary, the latest rupture of the southern branch dates back to the fifteenth century (Ambraseys, 2002). The fault delineates three tectonic blocks (Figure 1b): (a) the Istanbul Zone (IZ) situated North of the northern branch, (b) the Sakarya zone (SZ) situated to the South of the southern branch and (c) the Armutlu-Almacik crustal block (AA) located in the center, between the two fault strands (Chen et al., 2002; Okay & Tüysüz, 1999; Yılmaz et al., 1995). Differences in crustal composition and properties between these blocks have been reported. Strong velocity contrasts were found across the fault strands by several tomographic studies (Koulakov et al., 2010; Papaleo et al., 2017, 2018; Salah et al., 2007) and full waveform inversion studies (Çubuk-Sabuncu et al., 2017; Fichtner et al., 2013). Low velocity zones are found below the surface traces of the SNAFZ and NNAFZ (Papaleo et al., 2017, 2018). The crust of Istanbul and Armutlu Blocks is characterized by high velocities while SZ shows relatively low velocities (Koulakov et al., 2010; Papaleo et al., 2017, 2018; Taylor et al., 2019).

The present study reveals the 3D scattering structure of the medium below this major fault. It does not only image planar interfaces, but provides a direct insight on the heterogeneities that mainly sit in the vicinity of the strands. The observed results complement previous studies conducted in the region. A step in the Moho is detected below the Northern branch, and several sub-Moho structures are observed in the North confirming that the northern branch penetrates in the upper mantle. The southern strand does not have a strong signature in the scattering profiles.

2. Passive Seismic Matrix Imaging

2.1. Reflection Matrix in the Geophones Basis

To apply matrix imaging, we used the ambient seismic noise recorded at DANA (see Figure 1) to compute the cross-correlation functions of horizontal EE component over the 18 months of recording period. The choice of

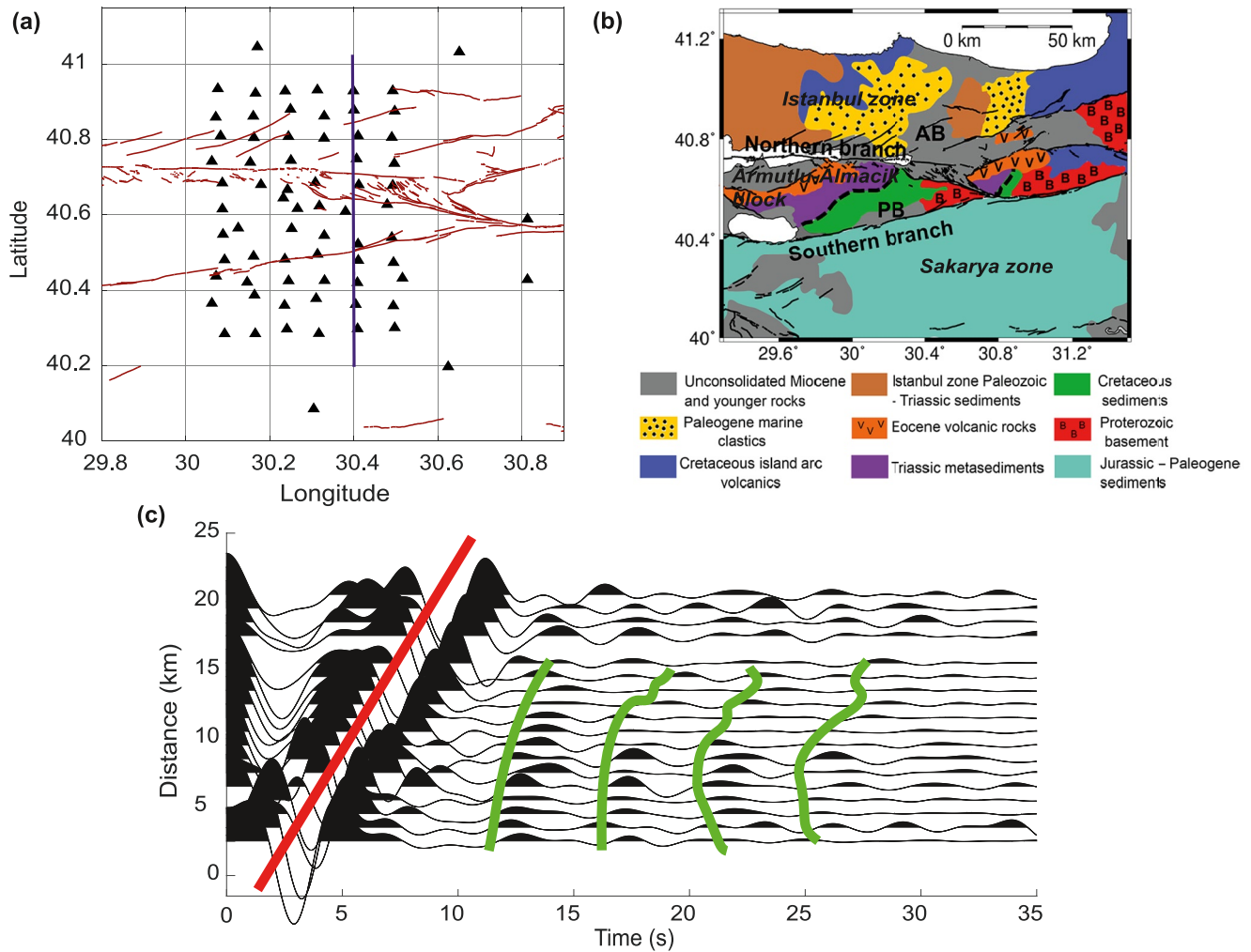


Figure 1. Study region and location of DANA array (DANA, 2012). (a) Map of the study region and location of DANA array geophones (black triangle). The surface traces of the North Anatolian Fault zone are represented by the red lines (Emre et al., 2018). The blue line indicate the location of the cross sections represented in Figures 4a and 8a. (b) Geological map of the region (adjusted from Taylor et al. (2019) and Akbayram et al. (2016)). The major geological blocks are represented: Istanbul zone (IZ) in the North, Armutlu-Almacik (AA) block in the center and Sakarya zone (SZ) in the South. The Adapazari and Pamukova basin location are indicated by AB and PB, respectively. (c) Ambient noise EE cross-correlation filtered between 0.1 and 0.5 Hz. The correlations between pairs of stations located South of the SNAF and having at least an angle of 45° with the East-West direction are plotted. These cross-correlograms are stacked over different distances. The predominant surface wave contribution and shear wave echoes induced by planar reflectors in the subsurface are highlighted by red and green lines, respectively.

the EE component is made because it displays a better signal-to-noise than the NN component. With this choice of body wave component, the waves being dealt with are mostly shear waves that have been reflected in depth. First, the data were down-sampled at 25 Hz and corrected from instrument response. Then, the data were split into one-hour windows. Each window is band-pass filtered between 0.1 and 0.5 Hz after applying a spectral whitening between 0.01 and 1 Hz (Bensen et al., 2007). The cross-correlation between each pair of stations is computed over 1-hour windows and finally stacked to obtain the mean cross-correlation function with time lags ranging from -35 to +35 s. The causal and the anti-causal parts of the cross-correlations are then summed in order to improve the convergence toward the Green's functions between seismic stations. Although, considering seismic noise in a higher frequency range would allow, in principle, to improve the resolution of the images, matrix imaging requires the Nyquist criterion to be fulfilled: The inter-station distance (7 km) shall be of the order of a half-wavelength. Considering a S-wave velocity $c_0 = 1,700$ m/s near the surface, this criterion led us to choose the 0.1–0.5 Hz frequency range ($\lambda = 5.7$ km at the central frequency, with λ the wavelength at the Earth surface). The ambient noise energy in the frequency band considered in this study comes from the secondary microseisms (5–10 s period band) produced in the ocean (Hasselmann, 1963; Longuet-Higgins, 1950; Stehly et al., 2006) and constitutes one of the most energetic parts of the seismic noise.

The symmetric cross-correlations can be stacked in a time-dependent response matrix $\mathbf{R}_{ss}(t)$. One element $R(\mathbf{s}_i, \mathbf{s}_j, t)$ of this matrix corresponds to the impulse response between geophones located at positions \mathbf{s}_i and \mathbf{s}_j . In other words, $R(\mathbf{s}_i, \mathbf{s}_j, t)$ contains the seismic wave-field recorded at receiver \mathbf{s}_i if a pulse was emitted by the virtual source \mathbf{s}_j at time $t = 0$. In the following, we will thus refer to columns and lines of the response matrix as input and output wave-fields, respectively.

Figure 1c shows the impulse responses between pairs of stations located South of the SNAF and having at least an angle of 45° with the East-West direction because of the EE polarization considered in this study. These responses are stacked for different inter-station distances. Figure 1c is dominated by surface-wave energy traveling at about 3,000 m/s. Given the horizontal polarization of seismic waves considered here, these surface waves correspond to Love waves. Interestingly, some nearly vertical weaker events are also observed at larger times. Due to their horizontal polarization, they correspond to shear waves reflected by the subsurface heterogeneities in depth.

Another way to highlight the surface and bulk wave components is to investigate the response matrix \mathbf{R}_{ss} in the frequency domain. To this aim, a temporal Fourier transform is applied to $\mathbf{R}_{ss}(t)$. For each frequency f in the bandwidth of interest (0.1–0.5 Hz), a monochromatic matrix $\bar{\mathbf{R}}_{ss}(f)$ is obtained. The different wave components can then be discriminated by a plane wave decomposition of the output wave-fields, such that

$$\bar{\mathbf{R}}_{sk}(f) = \bar{\mathbf{R}}_{ss}(f) \times \mathbf{P}_0, \quad (1)$$

where the symbol \times stands for the standard matrix product. $\mathbf{P}_0 = [P_0(\mathbf{s}, \mathbf{k})]$ is the Fourier transform operator that connects each geophone's position \mathbf{s} to the transverse wave vector $\mathbf{k} = (k_x, k_y)$ of each angular component of the wave-field:

$$P_0(\mathbf{s}, \mathbf{k}) = \exp(i\mathbf{k} \cdot \mathbf{s}), \quad (2)$$

where the symbol \cdot denotes the scalar product. Figure 2a shows the result of this plane wave decomposition by displaying the mean angular distribution of the output wave-field at $f_0 = 0.2$ Hz. More precisely, this distribution is displayed as a function of the ratio between spatial frequencies $k_x/(2\pi)$ and $k_y/(2\pi)$ and frequency f . In that representation, surface waves emerge along a circle whose radius should correspond to the slowness c_L^{-1} of Love waves, with $c_L \sim 3,000 \text{ m s}^{-1}$ (Taylor et al., 2019). On the other hand, reflected bulk waves are distributed over a disk of radius c_0^{-1} .

Figure 2a clearly reveals: (a) The contribution of Love waves with a dominant intensity lying along the y -direction; (b) A bulk wave component arising at small spatial frequencies and corresponding to the nearly vertical echoes already highlighted by Figure 1c. The latter contribution is a priori induced by extended reflectors in depth. On the contrary, diffuse scattering can generate reflected waves over a larger distribution of angles. It can therefore account for the incoherent background observed in Figure 2a. This background could result from the averaging of the random speckle pattern exhibited by the angular distribution of the reflected wave-field when only a few sources are considered (Figure 2b). Nevertheless, it is difficult at this stage to be more affirmative since an imperfect convergence of noise correlations could also lead to such a random wave-field.

A redatuming process is thus required to enhance the weight of scattered shear waves from seismic noise correlations and image the reflectivity of the deep structures around the NAFZ.

2.2. Redatuming Process

An image of the medium reflectivity can be obtained by applying a double focusing operation to \mathbf{R}_{ss} (Blondel et al., 2018; Touma et al., 2021). It consists in back-propagating the response measured at the surface into wave-fields below the surface as if there were sources and receivers inside the medium. This is similar to the “wave-field extrapolation” concept that forms the basis of the migration process (Berkhout, 1981). It requires performing beamforming operations both at emission and reception. On the one hand, focusing in emission consists in applying appropriate time delays to the emitting sources so that waves constructively interfere and focus on one point inside the medium. Physically, this operation amounts to synthesizing a virtual source inside the medium. On the other hand, focusing in reception is carried out by applying proper time delays to the received signals so that they can constructively interfere. As in emission, this focusing operation can be seen as the synthesis of a virtual receiver inside the medium. This operation is known as “redatuming” in seismology (Berkhout & Wapenaar, 1993) and consists of virtually moving sources and receivers from the surface to the medium below

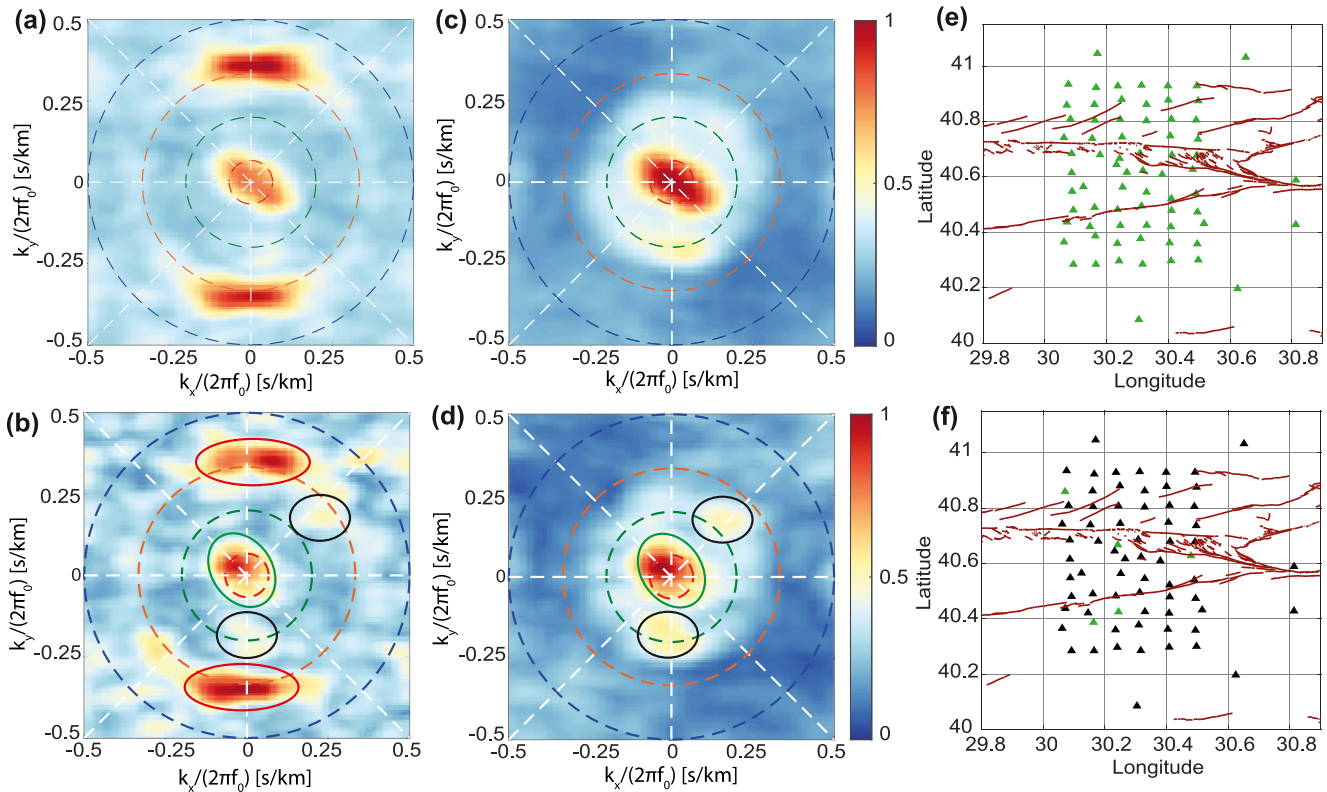


Figure 2. Apparent slowness of seismic echoes contained in the response matrix. (a, b) Plane wave decomposition of the Earth's response matrix \mathbf{R}_{ss} at output ($f_0 = 0.2$ Hz, Equation 1) averaged over the set of green geophones displayed in panels (e, f), respectively. (c, d) Plane wave decomposition of the filtered response matrix \mathbf{R}'_{ss} at output ($f_0 = 0.2$ Hz, $z = 25$ km, Equation 9) averaged over the set of green geophones in panels (e, f), respectively. The dashed circles correspond to apparent velocities of 5,000 m/s (green), 3,000 m/s (red) and 2,000 m/s (blue). Main echoes associated with Love waves (red ellipse), vertical shear waves (green ellipse) and off-axis shear waves (blue circle) are also highlighted in panels (b, d).

(Figure 3a). Generally, an image of the sub-surface is built by considering the response of virtual source and receiver placed at the same location (Figure 3f). On the other hand, the principle of matrix imaging consists in decoupling both locations (Lambert, Cobus, Couade, et al., 2020).

In the following, the reflection matrix will be expressed in three different bases: (a) the geophones basis where the matrix \mathbf{R}_{ss} represents the cross-correlations between all pairs of stations located at $\mathbf{s}(x_s, y_s, 0)$, (b) the focused basis corresponding to the location $\mathbf{r}(x, y, z)$ of virtual sources and receivers synthesized by the focusing operations and in which the image of the medium is built, and (c) the spatial Fourier basis $\mathbf{k} = (k_x, k_y)$ that will be first used for wave-field extrapolation and then for aberration correction.

2.3. Propagator From the Geophones to the Focused Basis

The focusing operations described in Section 2.2 provide the FR matrix that plays a pivotal role in matrix imaging. We now show how this matrix can be obtained through simple matrix operations.

Mathematically, the response between virtual sources and receivers is obtained from the response matrix at the surface through the Green's functions, that describe the propagation between each geophone and each point inside the medium using a wave velocity model. Switching between bases can be easily achieved by simple matrix products in the frequency domain. We first define the plane-wave propagator $\mathbf{T}_0(z, f)$, that enables a direct projection of the response matrix from the geophones' basis to the focused basis $\rho = (x, y)$ at each depth z . Each monochromatic response matrix $\bar{\mathbf{R}}_{ss}(f)$ can be projected in the focused basis both at input and output by applying appropriate phase shifts associated with downgoing waves at input and upgoing waves at output to provide the FR matrix $\bar{\mathbf{R}}_{\rho\rho}$ (Figure 3a). Under a matrix formalism, this operation can be written as follows:

$$\bar{\mathbf{R}}_{\rho\rho}(z, f) = \mathbf{T}_0^\dagger(z, f) \times \bar{\mathbf{R}}_{ss}(f) \times \mathbf{T}_0^*(z, f). \quad (3)$$

where the symbols * and † stands for phase conjugate and transpose conjugate, respectively.

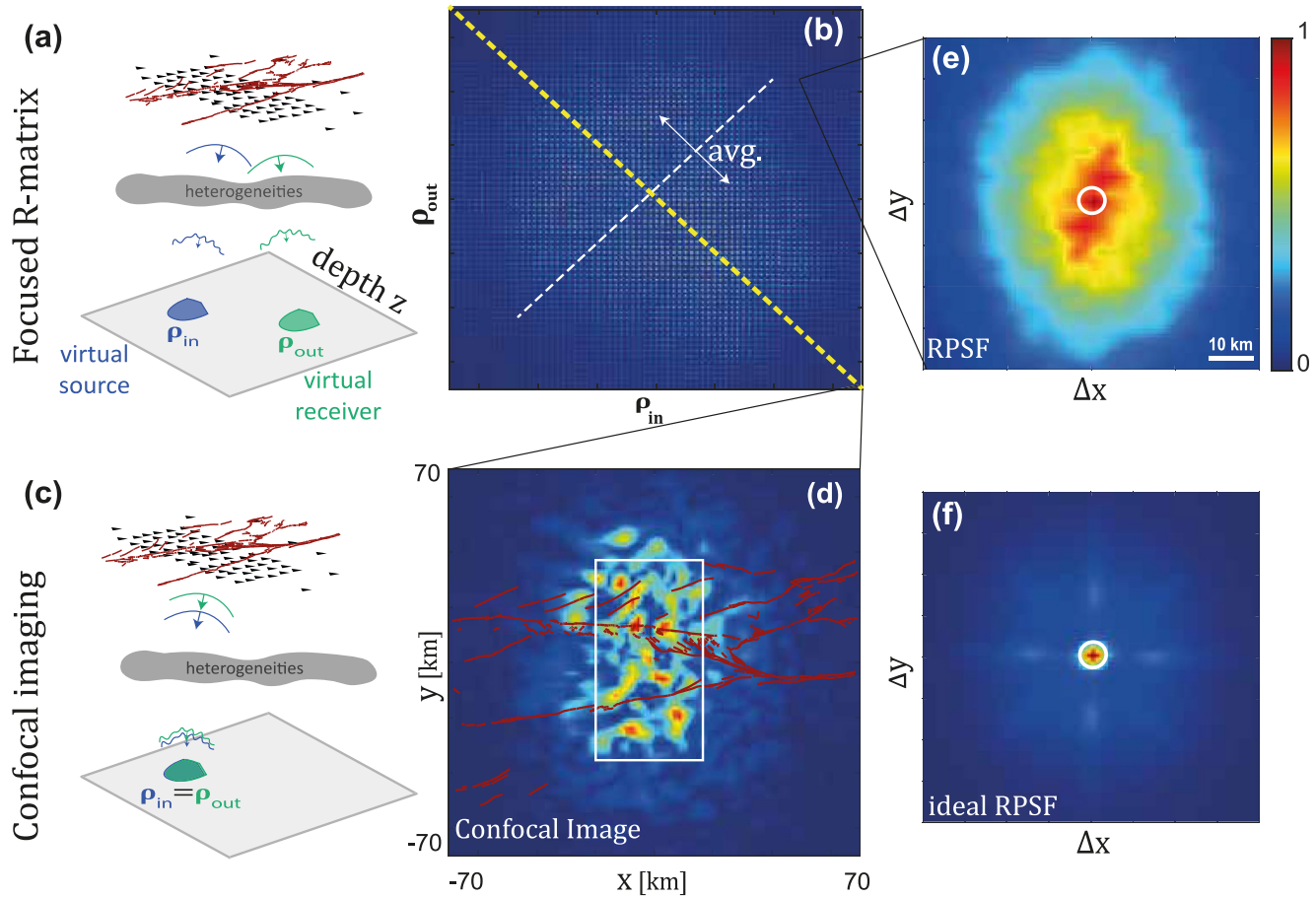


Figure 3. Focused reflection (FR) matrix. (a) The response matrix \mathbf{R}_{ss} is projected onto a focused basis at each depth z (Equation 10), thereby synthesizing a set of virtual sources (ρ_{in}) and receivers (ρ_{out}) scanning laterally the field-of-view. In presence of fluctuations in the seismic velocity, focused waves are distorted while traveling from the surface to the plane, thereby enlarging and distorting the virtual geophones. (b) This effect gives rise to an off-diagonal spreading of backscattered energy in the FR matrix $\mathbf{R}_{\rho\rho}(z)$ shown here at depth $z = 25$ km. (c) The corresponding intensity profile, averaged over whole the field-of-view, provides the so-called RPSF I (Equation 16). The white circle represents the diffraction-limited transverse resolution ($\delta\rho_0 \sim 6$ km) at the considered depth. (d) The ideal RPSF that would be obtained in absence of aberrations is shown for comparison. (e) Confocal image I (Equation 13) built from the diagonal of $\mathbf{R}_{\rho\rho}$. The white box represents the dimensions of the rectangular array of geophones and the red lines represent the North Anatolian Fault zone fault traces at the surface. (f) The confocal image corresponds to a simultaneous focusing process at input and output ($\mathbf{r}_{in} = \mathbf{r}_{out}$). In panels (b–e), the color scale refers to the scattering intensity. It is normalized by the maximum value of the scattering energy at the considered depth.

A model for the wave velocity distribution inside the medium is required. In this study, and since the horizontal EE cross-correlation functions are considered, only an estimate of the S-wave velocity is required. Unlike Blondel et al. (2018) and Touma et al. (2021) that considered a homogeneous P-wave velocity model, here a layered 1-D S-wave velocity model is used for the focusing process. A combination of two models derived by Kahraman et al. (2015), for the first 5 km, and by Karahan et al. (2001), for deeper layers is displayed in Table 1. Compared to an homogeneous model, such a layered model will allow better time-depth conversion and will limit the aberration level in the subsurface image. Note, however, that our wave propagation model will not account for multiple reflections that could, in principle, take place between the interfaces of the different layers.

In a layered medium, the forward and backward extrapolation of the reflection matrix can be performed through the decomposition of the wave-field into plane waves (Berkhout, 1981). Indeed, plane waves can be easily extrapolated by applying a simple phase shift.

Table 1
1-D S-Wave Velocity Model

Layer # <i>i</i>	Depth (km)	c_i (m s ⁻¹)
0	0–1	1,700
1	1–3.5	2,500
2	3.5–14	3,200
3	14–26	3,500
4	26–40	3,600
5	40–60	4,300

Note. c_i versus depth following Karahan et al. (2001) and Kahraman et al. (2015).

To that aim, we define the spatial transfer function, $F_i(\mathbf{k}, f)$, that models the ballistic propagation of shear waves through the i th layer:

$$F_i(\mathbf{k}, f) = \begin{cases} \exp(-iq_i \Delta z_i) & \text{for } \sqrt{k_x^2 + k_y^2} < 2\pi f / c_i, \\ 0 & \text{otherwise} \end{cases}, \quad (4)$$

with

$$q_i = \sqrt{\left(\frac{2\pi f}{c_i}\right)^2 - k_x^2 - k_y^2},$$

the vertical component of the wave vector $\mathbf{p}_i = (k_x, k_y, q_i)$ in the i th layer, c_i the wave velocity in the i th layer of our model and Δz_i its thickness. To propagate the plane waves from the surface to depth z , we define the wave-field extrapolator, $\mathbf{F}(z, f) = [F(\mathbf{k}, z, f)]$, as the product of the spatial transfer functions of the N layers above the considered depth as follows:

$$F(\mathbf{k}, z, f) = \begin{cases} \exp(-iq_N(z - z_N)) \prod_{i=1}^{N-1} F_i(\mathbf{k}, f) & \text{for } \sqrt{k_x^2 + k_y^2} < 2\pi f / c_N, \\ 0 & \text{otherwise.} \end{cases}, \quad (5)$$

where z_i is the depth at which starts the i th layer. The phase propagator, $\mathbf{T}(z, f) = [T(\mathbf{s}, \rho, z, f)]$, can finally be expressed as follows:

$$\mathbf{T}_0(z, f) = [\mathbf{P}_0 \circ \mathbf{F}(z, f)] \times \mathbf{P}'_0{}^\dagger. \quad (6)$$

where the symbol \circ refers to the Hadamard product (i.e., element wise matrix multiplication). In the Equation 6, the term-by-term product arises because wave propagation in the plane wave basis is modeled by the scalar product of each plane wave component $P_0(\mathbf{k}, \mathbf{s})$ with the overall spatial transfer function $F(\mathbf{k}, z)$. The matrix multiplication stands for the inverse Fourier transform that enables us to project the propagated wave-field from the plane wave basis to the focused basis. $\mathbf{P}'_0 = [P'_0(\rho, \mathbf{k})]$ is actually the Fourier transform operator linking the focused and plane wave bases. It connects the transverse wave vector $\mathbf{k} = (k_x, k_y)$ of each plane wave to the transverse coordinates $\rho = (x, y)$ of each focusing point:

$$\mathbf{P}'_0(\rho, \mathbf{k}) = \exp(i\mathbf{k} \cdot \rho). \quad (7)$$

To avoid aliasing during the change of basis between the plane wave and focused bases, a Shannon criterion should be respected. The transverse wave components, k_x and k_y , are required to fulfill the following condition:

$$\sqrt{k_x^2 + k_y^2} < 2\pi f / c_0. \quad (8)$$

The resolution δk of the Fourier plane is conditioned by the size of the array $D = 50$ km such that $\delta k = 2\pi / D$. By properties of the Fourier transform, the transverse resolution $\delta \rho_0$ in the focal plane, that corresponds to the distance between the focusing points ρ , is chosen to be $\lambda / 2 \sim 2$ km to circumvent spatial aliasing in the focused basis.

As shown by Equation 5, wave components of spatial frequencies larger than the wavenumber $2\pi f / c_i$ cannot be transmitted through the i th layer. As a consequence, redatuming acts as a low-pass filter in the spatial frequency domain. To illustrate this phenomenon, one can back-project the FR matrix in the geophone basis,

$$\overline{\mathbf{R}}'_{ss}(f) = \mathbf{T}_0(z, f) \times \overline{\mathbf{R}}_{\rho\rho}(z, f) \times \mathbf{T}_0^\top(z, f), \quad (9)$$

where the superscript \top stands for matrix transpose. From $\overline{\mathbf{R}}'_{ss}(f)$, one can investigate the angular decomposition of the output wave-fields as previously done for the original response matrix $\overline{\mathbf{R}}_{ss}$ in Figures 2a and 2b (Equation 1). The result is displayed in Figures 2c and 2d. The comparison with their original counterparts highlights the low pass-filter operated by redatuming: The surface wave component is discarded and only the shear waves associated with spatial frequencies $k < 2\pi f / c_N$ are kept. Figure 2d displays: (a) a low-spatial frequency component associated with specular reflectors; (b) several off-axis bright spots associated with peculiar single scattering events at depth z and; (c) a diffuse background that is difficult to interpret at this stage since it can be due to random single

scattering, multiple scattering or noise resulting from the imperfect convergence of cross-correlations toward the Green's function. To enhance the single scattering contribution with respect to the other undesirable components for imaging, the idea is now to perform a time gating operation to enhance the single scattering contribution.

2.4. Broadband Focused Reflection Matrix

Equation 3 simulates focused beamforming for both downgoing (input) and upgoing (output) shear waves at each frequency. Each spectral component of the wave-field can then be recombined to provide a broadband FR matrix $\overline{\mathbf{R}}_{\rho\rho}(z)$:

$$\overline{\mathbf{R}}_{\rho\rho}(z) = \int_{f_1}^{f_2} df \overline{\mathbf{R}}_{\rho\rho}(z, f), \quad (10)$$

with $f_1 = 0.1$ Hz and $f_2 = 0.5$ Hz. This operation amounts to performing an inverse Fourier transform at time $t = 0$ over the frequency band $[0.1 \text{ } 0.5]$ Hz. Note that this inverse Fourier transform is only performed over positive frequencies in order to have access to both the amplitude and phase of the wave-field. The time origin here corresponds to the ballistic time in the focused basis. Equation 10 thus corresponds to a time gating operation that tends to select singly scattered waves associated with a scattering event in the focal plane. Each coefficient $R(\rho_{\text{out}}, \rho_{\text{in}}, z)$ of $\mathbf{R}_{\rho\rho}(z)$ contains the complex wave-field that would be recorded by a virtual geophone located at $\mathbf{r}_{\text{out}} = (\rho_{\text{out}}, z)$ if a virtual source at $\mathbf{r}_{\text{in}} = (\rho_{\text{in}}, z)$ emits a pulse of length $\delta t = \Delta f^{-1}$ at the central frequency f_0 , with $\Delta f = f_2 - f_1 = 0.4$ Hz.

The FR matrix can be expressed theoretically as follows (Lambert, Cobus, Couade, et al., 2020; Lambert, Cobus, Frappart, et al., 2020; Touma et al., 2021),

$$\mathbf{R}_{\rho\rho}(z) = \mathbf{H}^T(z) \times \mathbf{\Gamma}(z) \times \mathbf{H}(z), \quad (11)$$

which yields, in terms of matrix coefficients,

$$R(\rho_{\text{out}}, \rho_{\text{in}}, z) = \int d\rho H(\rho, \rho_{\text{out}}, z) \gamma(\rho, z) H(\rho, \rho_{\text{in}}, z). \quad (12)$$

The matrix $\mathbf{\Gamma}$ describes the scattering process in the focused basis. In the single scattering regime, this matrix is diagonal and its coefficients correspond to the subsurface reflectivity $\gamma(\rho, z)$ at depth z . $\mathbf{H}(z)$ is the focusing matrix whose coefficients $H(\rho, \rho_{\text{in/out}}, z)$ correspond to the point spread functions (PSFs) of the redatuming process. These PSFs represent the spatial amplitude distribution of the focal spots for each focusing point $\mathbf{r}_{\text{in/out}} = (\rho_{\text{in/out}}, z)$. They thus account for the lateral extent of each virtual source/detector at $\mathbf{r}_{\text{in/out}}$.

An example of the broadband FR matrix $\mathbf{R}_{\rho\rho}$ is shown at depth $z = 25$ km in Figure 3b. $\mathbf{R}_{\rho\rho}$ is a four-dimension matrix concatenated in 2D as a set of blocks (Blondel et al., 2018). If the wave velocity model was correct, the PSFs of the redatuming process would be close to be point-like [$H(\rho, \rho_{\text{in/out}}, z) \simeq \delta(\rho - \rho_{\text{in/out}})$, with δ the Dirac distribution] and the FR matrix $\mathbf{R}_{\rho\rho}$ almost diagonal [$R(\rho_{\text{out}}, \rho_{\text{in}}, z) \simeq \gamma(\rho_{\text{in}}) \delta(\rho_{\text{in}} - \rho_{\text{out}})$, see Equation 12]. Here, the backscattered energy is far from being concentrated along the diagonal of $\mathbf{R}_{\rho\rho}$, which is a manifestation of the gap between our layered wave velocity model (Table 1) and the real shear wave velocity distribution in the subsurface.

2.5. Confocal Image

Nevertheless, one can try to build an image of the medium reflectivity at each effective depth z by considering the diagonal elements of the FR matrix, that is, where the virtual sources and receivers coincide ($\rho_{\text{in}} = \rho_{\text{out}} = \rho_c$, see Figure 3c). It yields the so-called *confocal* image:

$$\mathcal{I}(\rho_c, z) = R(\rho_c, \rho_c, z). \quad (13)$$

Figure 3e shows the resulting 2D image \mathcal{I} at $z = 25$ km retrieved from the diagonal of the FR matrix in Figure 3b. By injecting Equation 12 into the last equation, \mathcal{I} can be expressed as the transverse convolution between the medium reflectivity and the confocal PSF H^2 , such that:

$$\mathcal{I}(\rho_c, z) = \int d\rho \gamma(\rho, z) H^2(\rho, \rho_c, z). \quad (14)$$

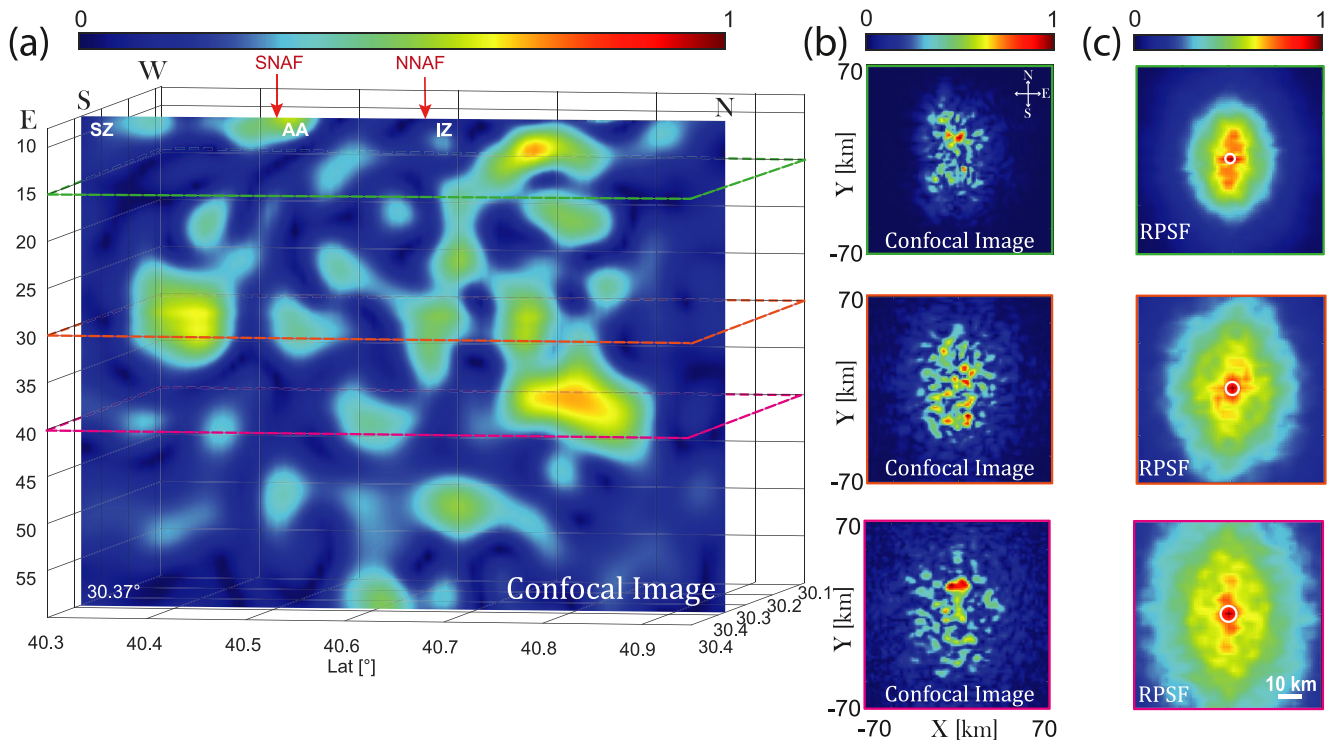


Figure 4. Original confocal image of North Anatolian Fault zone. (a) Vertical North-South cross-section at 30.37°E. The North-South profile is oriented perpendicular to the fault traces. The location of the profile is shown in Figure 1a. The locations of the southern (SNAF) and northern (NNAF), and the major crustal blocks (SZ: Sakarya zone, AA: Armutlu-Almacik and IZ: Istanbul zone) are labeled. The color scale refers to the scattering intensity. It is normalized by the maximum value of the scattering energy inside the volume. (b) Depth slices retrieved from the 3D scattering volume at $z = 15, 30$ and 40 km with (c) their corresponding RPSFs.

Such an image is thus a reliable estimator of the reflectivity at depth z only if the wave velocity model is close to reality. In this ideal case, the spatial extent of the PSF is only limited by diffraction and the transverse resolution is given by Born and Wolf (2003):

$$\delta\rho_0 = \lambda / (2 \sin \theta) \quad (15)$$

where $\theta = \arctan(D/2z)$ is determined by the size of the array $D = 50$ km, and corresponds to the maximum angle under which a focusing point sees the geophones' array.

By stacking the confocal image computed at each depth z , a 3D image of the reflectivity can be obtained. The cross-section at Lon 30.37° is displayed in Figure 4a. 2D *confocal* images at $z = 15, 30$ and 40 km are also shown in Figure 4b. Unlike the transverse resolution, the axial resolution δz is limited by the frequency bandwidth: $\delta z \sim c/\Delta f \sim 8.7$ km, with c the shear wave velocity at the considered depth. The sections of the 3D image displayed in Figures 3e, 4a, and 4b show a greater reflectivity in the central part of the field-of-view, that is, right below the geophones' array, but no direct correlation can be found between the image and the location of the fault strands. In fact, as we will see now, lateral wave speed heterogeneities strongly degrade the transverse resolution of the redatuming process and induce strong aberrations in the confocal image. This image is thus not a reliable estimator of the medium reflectivity at this stage and cannot be interpreted.

2.6. Quantification of Aberrations

The FR matrix can provide more than a confocal image since its off-diagonal elements can lead to a quantification of aberrations. To that aim, a relevant observable is the distribution of the backscattered intensity around a common midpoint point (ρ_m, z) as a function of the relative position, $\Delta\rho = \rho_{out} - \rho_{in}$, between the input and output focusing points (Lambert, Cobus, Couade, et al., 2020; Touma et al., 2021):

$$I(\Delta\rho, \rho_m, z) = |R(\rho_m - \Delta\rho/2, \rho_m + \Delta\rho/2, z)|^2. \quad (16)$$

In the following, we will refer to this quantity as the reflection point spread function (RPSF).

To express this quantity theoretically, we first make a local isoplanatic approximation in the vicinity of each point (ρ_m, z) (Lambert, Robin, et al., 2022). Isoplanaticity means here that waves which focus in this region are assumed to have traveled through approximately the same areas of the medium, thereby undergoing identical phase distortions. The PSF can then be considered to be spatially invariant within this local region. Mathematically, this means that, in the vicinity of each point (ρ_m, z) , the spatial distribution of the PSF, $H(\rho, \rho_{\text{in/out}}, z)$, only depends on the relative distance between the point ρ and the focusing point $\rho_{\text{in/out}}$. This leads us to define a local spatially-invariant PSF H_L around each common mid-point (ρ_m, z) such that:

$$H(\rho, \rho_{\text{in/out}}, z) = H_L(\rho - \rho_{\text{in/out}}, \rho_m, z). \quad (17)$$

Under this local isoplanatic assumption, the RPSF can be derived analytically in different scattering regimes. On the one hand, for large reflectors such as horizontal interfaces between geological units, the medium reflectivity can be assumed as locally constant and the RPSF is given by (see Text S1 in Supporting Information S1):

$$I(\Delta\rho, \rho_m, z) = |\gamma(\rho_m, z)|^2 \left| H_L \overset{\Delta\rho}{\otimes} H_L \right|^2 (\Delta\rho, \rho_m, z). \quad (18)$$

where the symbol \otimes denotes convolution. On the other hand, for diffuse scattering, the medium reflectivity can be considered, in first approximation, as randomly distributed. Under that assumption, the mean RPSF is then proportional to the convolution between the incoherent output and input local PSFs, independently from the medium's reflectivity (Lambert, Cobus, Couade, et al., 2020) (see Text S1 in Supporting Information S1):

$$\langle I(\Delta\rho, \rho_m, z) \rangle \propto \left[|H_L|^2 \overset{\Delta\rho}{\otimes} |H_L|^2 \right] (\Delta\rho, \rho_m, z) \quad (19)$$

where the symbol $\langle \dots \rangle$ stands for an ensemble average. Whatever the scattering regime, the spatial extension of the RPSF is thus roughly equal to the lateral dimension of the PSF. If we assume a Gaussian PSF, this equality is strict. The RPSF is thus a direct indicator of the focusing quality and its spatial extent directly provides an estimation of the local transverse resolution of the confocal image.

Figure 3c displays the RPSF averaged over the whole field-of-view at depth $z = 25$ km. For sake of comparison, Figure 3d shows the ideal (i.e., diffraction-limited) RPSF that would be obtained in absence of aberrations. The comparison between Figures 3c and 3d highlights the impact of aberrations resulting from the mismatch between the wave velocity model of Table 1 and the real wave speed distribution. Indeed, the full width at half maximum w of the intensity profile is increased by a factor ~ 6 compared to its diffraction-limited value (white circle in Figure 3d, Equation 15) at depth $z = 25$ km. This effect explains the blurred aspect of the confocal image displayed in Figure 3e at the same depth. The impact of aberrations is also illustrated by Figure 4c that displays the depth evolution of the RPSF inside the Earth. As with the diffraction-limited resolution (Equation 15), the transverse extension of the RPSF also increases with z but it shows a much larger extension.

In the following we will show how matrix imaging can restore an optimal resolution for this image.

3. Exploiting the Input-Output Angular Correlations of the Wave-Field: The CLASS Algorithm

In order to compensate for aberrations, the reflection matrix can be first projected in the plane wave basis:

$$\mathbf{R}_{\mathbf{k}\mathbf{k}}(z) = \mathbf{P}'_0 \times \mathbf{R}_{\rho\rho}(z) \times \mathbf{P}'_0{}^T, \quad (20)$$

Using Equation 7, the last equation can be rewritten, in terms of matrix coefficients, as a double spatial Fourier transform:

$$R(\mathbf{k}_{\text{out}}, \mathbf{k}_{\text{in}}, z) = \sum_{\rho_{\text{out}}} \sum_{\rho_{\text{in}}} e^{-i\mathbf{k}_{\text{out}} \cdot \rho_{\text{out}}} R(\rho_{\text{out}}, \rho_{\text{in}}, z) e^{-i\mathbf{k}_{\text{in}} \cdot \rho_{\text{in}}} \quad (21)$$

Each coefficient of the matrix $\mathbf{R}_{\mathbf{k}\mathbf{k}}(z) = [R(\mathbf{k}_{\text{out}}, \mathbf{k}_{\text{in}}, z)]$ thus contains the medium response between input and output transverse wave vectors \mathbf{k}_{in} and \mathbf{k}_{out} . By injecting Equation 11 into Equation 20, the matrix $\mathbf{R}_{\mathbf{k}\mathbf{k}}$ can be expressed as follows:

$$\mathbf{R}_{\mathbf{k}\mathbf{k}}(z) = \mathbf{T}(z) \times \mathbf{\Gamma}(z) \times \mathbf{T}^{\text{T}}(z), \quad (22)$$

where $\mathbf{T}(z) = \mathbf{P}'_0 \times \mathbf{H}(z)$ is the transmission matrix describes plane wave propagation between the focused and the plane wave bases. Its coefficients $T(\mathbf{k}, \rho, z)$ correspond to the angular decomposition of the wave-field produced at the Earth surface for a point-like virtual source located at (ρ, z) . This matrix is critical for imaging since its inversion can provide a direct access to the subsurface reflectivity, without relying on a precise wave velocity model.

As a first step toward the estimation of \mathbf{T} , we can go one step further in the isoplanatic approximation (Equation 17) by assuming a full transverse-invariance of the PSF across the field-of-view. This leads us to define a laterally invariant PSF H_I , such that:

$$H_L(\rho - \rho_{\text{in/out}}, \rho_m, z) \simeq H_I(\rho - \rho_{\text{in/out}}, z). \quad (23)$$

This strong assumption means that wave speed heterogeneities are modeled by a phase screen of transmittance $\tilde{\mathbf{H}}_I = [\tilde{H}_I(\mathbf{k}, z)]$ in the plane wave basis, such that $\mathbf{T}(z) = \tilde{\mathbf{H}}_I(z) \circ \mathbf{P}'_0$, where $\tilde{H}_I(\mathbf{k}, z) = \int d\rho H_I(\rho, z) e^{-i\mathbf{k} \cdot \rho}$ is the Fourier transform of the spatially invariant PSF $H_I(\rho, z)$. The aberration transmittance $\tilde{\mathbf{H}}_I$ grasps the phase distortions undergone by downgoing and upgoing wave-fields during their travel between the Earth surface and the focal plane at effective depth z .

Under this full isoplanatic approximation (Equation 23), a theoretical expression of $\mathbf{R}_{\mathbf{k}\mathbf{k}}$ can be derived in the single scattering regime (Lambert, Cobus, Frappart, et al., 2020):

$$R(\mathbf{k}_{\text{out}}, \mathbf{k}_{\text{in}}, z) = \tilde{H}_I(\mathbf{k}_{\text{in}}, z) \tilde{\gamma}(\mathbf{k}_{\text{in}} + \mathbf{k}_{\text{out}}, z) \tilde{H}_I(\mathbf{k}_{\text{out}}, z), \quad (24)$$

where $\tilde{\gamma}(\mathbf{k}, z) = \int d\rho \gamma(\rho, z) \exp(-i\mathbf{k} \cdot \rho)$ is the 2D Fourier transform of the medium's reflectivity $\gamma(\rho, z)$ at each depth z . In absence of aberrations ($\tilde{H}_I(\mathbf{k}, z) \equiv 1$), the reflection matrix expressed in the plane wave basis exhibits a deterministic coherence along its antidiagonals ($\mathbf{k}_{\text{in}} + \mathbf{k}_{\text{out}} = \text{constant}$, see Figure 5c): $R(\mathbf{k}_{\text{in}}, \mathbf{k}_{\text{out}}, z) = \tilde{\gamma}(\mathbf{k}_{\text{in}} + \mathbf{k}_{\text{out}}, z)$ (Aubry & Derode, 2009; Kang et al., 2015). This peculiar property is a manifestation of a phenomenon called the memory effect in wave physics (Freund et al., 1988; Shahjahan et al., 2014). When an incident plane wave (\mathbf{k}_{in}) illuminates a scattering medium, it gives rise to a reflected wave-field (\mathbf{k}_{out}) that exhibits a speckle feature (Figure 5a) due to the random interference between partial waves induced by each scatterer lying at depth z . When this incident plane wave is rotated by a certain angle ($\mathbf{k}_{\text{in}} + \Delta\mathbf{k}$), the reflected wave-field is tilted in the opposite direction ($\mathbf{k}_{\text{in}} - \Delta\mathbf{k}$, see Figure 5b). This correlation between the downgoing and upgoing wave-fields accounts for the deterministic coherence along the antidiagonals of $\mathbf{R}_{\mathbf{k}\mathbf{k}}$ (Figure 5c). However, in the present case, this property is not checked because of the phase distortions undergone by downgoing and upgoing wave-fields induced by wave speed heterogeneities. Mathematically, this is accounted by the phase screen $\tilde{H}_I(\mathbf{k}, z)$ in Equation 24 that breaks the correlation between coefficients lying along the same antidiagonal (Figure 5d).

The principle of the CLASS algorithm (Choi et al., 2018; Kang et al., 2017; Yoon et al., 2020) consists in restoring this coherence by applying a phase correction, $\exp[-i\phi_C(\mathbf{k}, z)]$, to the input and output of $\mathbf{R}_{\mathbf{k}\mathbf{k}}$:

$$R^{(C)}(\mathbf{k}_{\text{out}}, \mathbf{k}_{\text{in}}, z) = e^{-i\phi_C(\mathbf{k}_{\text{out}}, z)} R(\mathbf{k}_{\text{out}}, \mathbf{k}_{\text{in}}, z) e^{-i\phi_C(\mathbf{k}_{\text{in}}, z)}, \quad (25)$$

where ϕ_C is the estimator of the aberration phase law whose phase conjugate maximizes the coherence along the antidiagonals of $\mathbf{R}_{\mathbf{k}\mathbf{k}}$. To compute ϕ_C , the first step is to perform a coherent sum of $\mathbf{R}_{\mathbf{k}\mathbf{k}}$'s coefficients along each of its antidiagonals (see Figure 5e):

$$C(\mathbf{k}_+, z) = \sum_{\mathbf{k}_{\text{out}}} R(\mathbf{k}_{\text{out}}, \mathbf{k}_+ - \mathbf{k}_{\text{out}}, z) \quad (26)$$

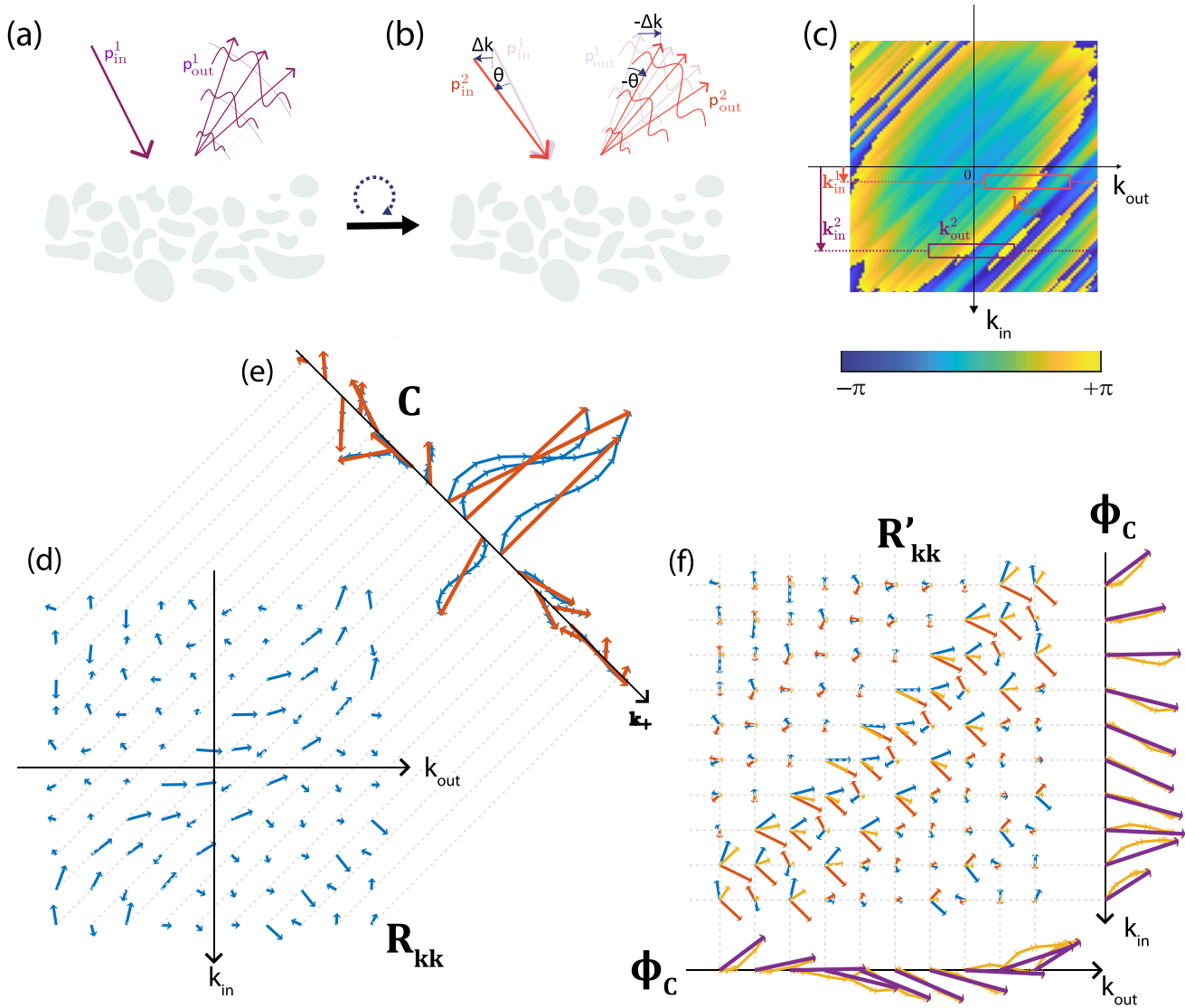


Figure 5. Principles of the memory effect and CLASS algorithm. (a) When an incident plane wave of wave vector \mathbf{p}_{in}^1 insonifies a scattering medium, the reflected wave-field exhibits a random speckle pattern. (b) When this incident wave-field is rotated by an angle θ , the reflected wave-field is shifted by the opposite angle $-\theta$: This is the so-called memory effect. (c) This phenomenon results in a deterministic coherence along the antiagonals ($\mathbf{k}_{in} + \mathbf{k}_{out} = \text{constant}$) of the reflection matrix \mathbf{R}_{kk} expressed in the plane wave basis. The phase of a matrix \mathbf{R}_{kk} is displayed for sake of illustration. This matrix has been obtained from an ultrasound experiment performed on a medium of random reflectivity (acoustic phantom) in the conditions described by Lambert, Cobus, Couade, et al. (2020). (d) Same matrix as in (c) but in presence of aberrations. Each complex coefficient of \mathbf{R}_{kk} is here represented by blue arrows using a Fresnel diagram. (e) The first step of CLASS (Equation 26) consists in a coherent sum of coefficients lying along the same anti-diagonal to estimate the spatial frequency spectrum $\tilde{\gamma}$ of the medium reflectivity. Each coefficient of the resulting vector \mathbf{C} is represented by a red arrow in the complex plane. (f) The second step of CLASS consists in a compensation of \mathbf{R}_{kk} by \mathbf{C}^* to compensate for the phase of reflectivity spectrum $\tilde{\gamma}$ (Equation 27). The coefficients of the resulting matrix \mathbf{R}'_{kk} are depicted with orange arrows. A sum over lines or columns of \mathbf{R}'_{kk} provides the isoplanatic aberrated wave-front $\exp(i\phi_c)$ represented by purple arrows (Equation 28).

with $\mathbf{k}_+ = \mathbf{k}_{in} + \mathbf{k}_{out}$. As shown in Text S2 in Supporting Information S1, $C(\mathbf{k}_+, z)$ is a rough estimator for the spatial frequency spectrum $\tilde{\gamma}(\mathbf{k}_+, z)$ of the medium reflectivity (see Text S2 in Supporting Information S1). The second step consists in performing the Hadamard product (element-wise product) between the phase conjugate of the vector \mathbf{C} and the matrix \mathbf{R}_{kk} (Figure 5f):

$$\mathbf{R}'(\mathbf{k}_{out}, \mathbf{k}_{in}, z) = \mathbf{R}(\mathbf{k}_{out}, \mathbf{k}_{in}, z) \mathbf{C}^*(\mathbf{k}_{out} + \mathbf{k}_{in}, z). \quad (27)$$

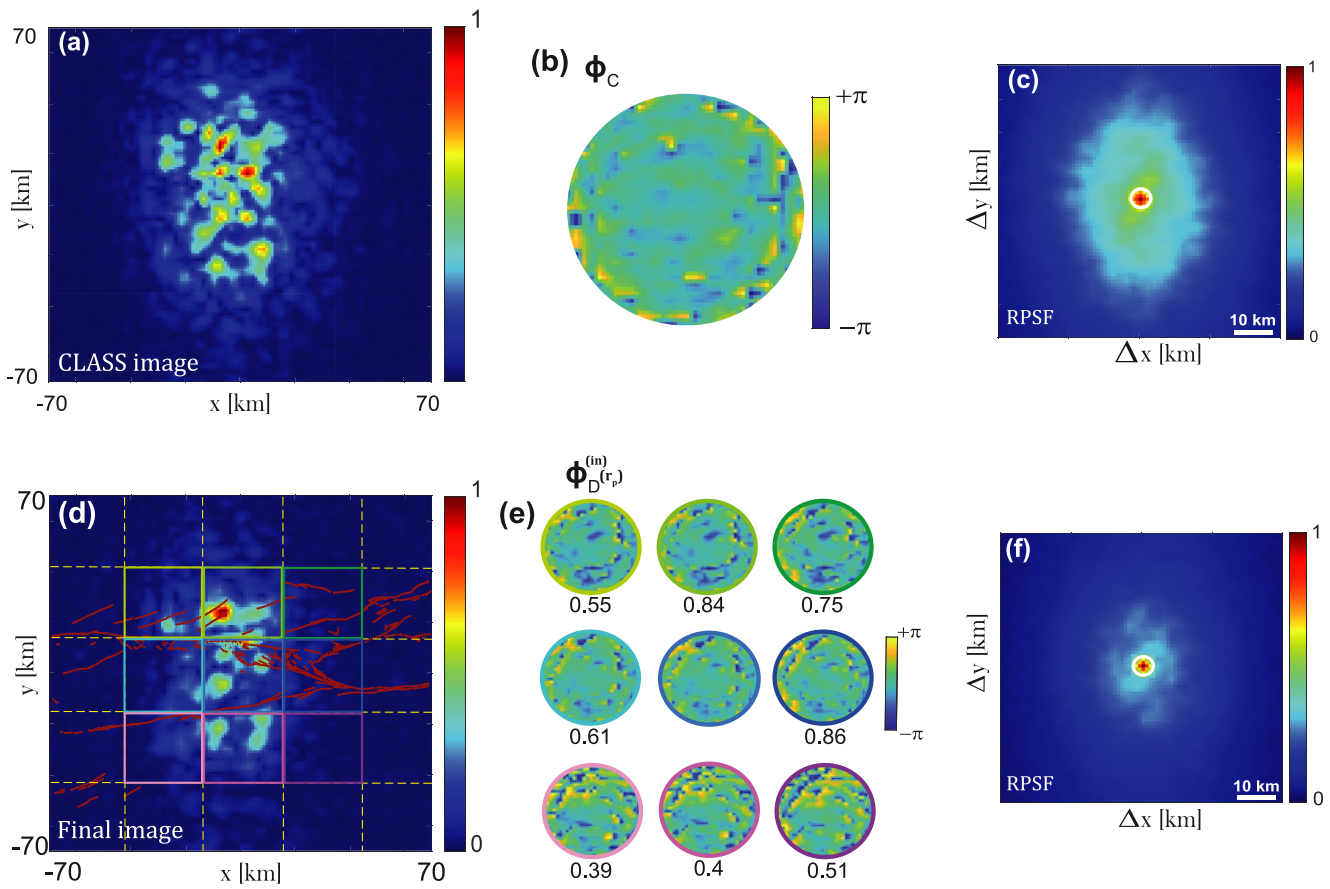


Figure 6. Aberration correction process at $z = 25$ km. (a) Confocal image obtained after applying the conjugate of (b) the CLASS phase law ϕ_C computed at this depth. (c) RPSF obtained after CLASS correction. (d) Confocal image obtained after performing four iteration steps of the distortion matrix process. The red lines represent the North Anatolian Fault zone fault traces at the surface. The yellow dashed lines delineate the regions over which a local aberration phase law $\phi(\mathbf{k}, \mathbf{r})$ has been estimated. (e) Corresponding input aberration phase laws $\phi_{in}(\mathbf{k}, \mathbf{r})$ obtained at the end of the process. The correlation coefficients between the corresponding aberration transmittances and the central one are displayed below each phase mask. (f) RPSF at the end of the matrix imaging process.

The last operation amounts to compensate for the phase fluctuations of the reflectivity spatial frequency spectrum $\tilde{\gamma}$ in \mathbf{R}_{kk} . The isoplanatic phase distortion $\tilde{\mathbf{H}}_I$ is finally estimated by summing the columns of the compensated matrix \mathbf{R}'_{kk} (see Figure 5f)

$$\phi_C(\mathbf{k}_{out}, z) = \arg \left[\sum_{\mathbf{k}_{in}} R'(\mathbf{k}_{out}, \mathbf{k}_{in}, z) \right], \quad (28)$$

The phase conjugate of the resulting wave-front, $\exp[-i\phi_C(\mathbf{k}, z)]$, tends to realign in phase the coefficients lying on the same antidiagonal of \mathbf{R}_{kk} (Equation 25). As shown in Text S2 in Supporting Information S1, this phase realignment in the plane wave basis is equivalent to a maximization of the confocal intensity in the focused basis.

The corresponding FR matrix $\mathbf{R}_{\rho\rho}^{(C)}$ can be deduced as follows:

$$\mathbf{R}_{\rho\rho}^{(C)}(z) = \mathbf{P}_0^{\dagger}(z) \times \mathbf{R}_{kk}^{(C)}(z) \times \mathbf{P}_0^*(z) \quad (29)$$

A corrected confocal image is extracted from the diagonal of $\mathbf{R}_{\rho\rho}^{(C)}(z)$ and displayed in Figure 6a at depth $z = 25$ km. It should be compared with the original image shown in Figure 3e. While the latter one displays a random-like feature, the corrected image reveals a greater reflectivity in the North that can be correlated with the expected damage around the Northern branch of the fault. The comparison between these two images illustrates the benefit of the correction process. The gain in resolution can be assessed by averaging the RPSF (Equation 16) over the whole field-of-view (see Figure 6c). Compared to the original RPSF displayed in Figure 3c,

we can notice that a large component of the off-diagonal energy has been brought back to the confocal lobe (white circle). The resolution w is reduced from 40 to 8 km but it is still larger than the diffraction-limited resolution ($\delta\rho_0 \sim 6$ km at the considered depth). A diffuse component subsists and can be explained by the spatially-varying residual aberrations, $\delta\tilde{H}_L(\mathbf{k}, \rho_m, z)$, that have not been compensated by the CLASS algorithm, such that $\delta\tilde{H}_L(\mathbf{k}, \rho_c, z) = \tilde{H}_L(\mathbf{k}, \rho_c, z)e^{-i\phi_C(\mathbf{k}, z)}$.

A local compensation of higher order aberrations is thus required. This issue is handled in the following section by investigating the reflection matrix and its distorted component between the focused and plane wave bases.

4. Matrix Approach for Adaptive Focusing: The Local Distortion Matrix

The distortion matrix \mathbf{D} was already introduced in ultrasound (Lambert, Cobus, Frappart, et al., 2020; Lambert, Cobus, Frappart, et al., 2020), optics (Badon et al., 2020; Najar et al., 2023) and seismology (Touma et al., 2021). Several applications proved the efficiency of this matrix in overcoming aberrations and improving the image quality. Recent works in seismology (Touma et al., 2021) and optics (Badon et al., 2020) have shown that for certain scattering regimes (specular reflectors or sparse scattering), there was a one-to-one association between the eigenstates of \mathbf{D} and the isoplanatic patches present in the field-of-view. Here, this property does not hold because the NAFZ subsurface exhibits a continuous but fluctuating reflectivity (see Text S3 in Supporting Information S1). In this scattering regime, local distortion matrices should be considered over restricted areas in which the isoplanatic hypothesis is ideally fulfilled (Lambert, Cobus, et al., 2022; Najar et al., 2023).

In this section, the distortion matrix concept is applied to the CLASS FR matrix obtained in the previous section for compensation of spatially-distributed aberrations. The process is outlined by five steps: (a) projection of the CLASS FR matrix at output into the plane wave basis (Figure 7a), (b) the realignment of the reflected wave-fronts to form a distortion matrix $\mathbf{D} = [D(\mathbf{k}_{\text{out}}, \rho_{\text{in}}, z)]$ (see Figure 7b), (c) the truncation of \mathbf{D} into local distortion matrices $\mathbf{D}'(\mathbf{r}_p)$, (d) the singular value decomposition of $\mathbf{D}'(\mathbf{r}_p)$ to extract a residual aberration phase law for each point \mathbf{r}_p and build an estimator $\hat{\mathbf{T}}$ of the transmission matrix \mathbf{T} (Figure 7c); (e) the phase conjugation of $\hat{\mathbf{T}}$ to correct for output residual aberrations (Figure 7d). All of these steps are then repeated by exchanging output and input bases.

4.1. The Distortion Matrix

The output of the CLASS algorithm is a FR matrix $\mathbf{R}_{\rho\rho}^{(C)}$ that still exhibits laterally-varying aberrations. To assess these residual aberrations, the first step is to choose a basis in which the distortion of the CLASS wave-front is the most spatially-invariant. In a horizontally multi-layered medium such as NAFZ, the plane-wave basis is the most adequate since plane waves are the propagation invariants in this geometry. A plane-wave projection is performed at the output of the CLASS FR matrix $\mathbf{R}_{\rho\rho}^{(C)}$:

$$\mathbf{R}_{\mathbf{k}\rho}^{(C)}(z) = \mathbf{P}'_0 \times \mathbf{R}_{\rho\rho}^{(C)}(z), \quad (30)$$

$\mathbf{R}_{\mathbf{k}\rho}^{(C)}(z) = [R^{(C)}(\mathbf{k}_{\text{out}}, \rho_{\text{in}}, z)]$ connects each input focusing point $\mathbf{r}_{\text{in}} = (\rho_{\text{in}}, z)$ to the CLASS wave-field in the plane wave basis (Figure 7a).

The CLASS wave-field can be understood as a sum of two components: (a) a geometrical component described by the reference matrix \mathbf{P}'_0 , containing the ideal wave-front generated by a source at \mathbf{r}_{in} according to the propagation model described in Table 1 (dashed black curves in Figure 7a); (b) a distorted component due to spatially-distributed aberrations that subsists after the CLASS procedure. The latter component refers to the residual phase distortions that should be isolated from the CLASS wave-field in order to be properly compensated. This can be done by subtracting the ideal wave-front that would be obtained in absence of aberrations (i.e., the geometrical component) from each CLASS wave-front induced by each input focusing wave at \mathbf{r}_{in} . Such operation can be expressed mathematically via a Hadamard product between $\mathbf{R}_{\mathbf{k}\rho}^{(C)}(z)$ and \mathbf{P}'_0 . It yields the residual distortion matrix $\mathbf{D}(z)$:

$$\mathbf{D}(z) = \mathbf{R}_{\mathbf{k}\rho}^{(C)}(z) \circ \mathbf{P}'_0, \quad (31)$$

The matrix $\mathbf{D}(z)$ connects any input virtual source \mathbf{r}_{in} to the residual distortion exhibited by the CLASS wave-field expressed in the plane wave basis (Figure 7b). By removing the geometrical component of the CLASS wave-field,

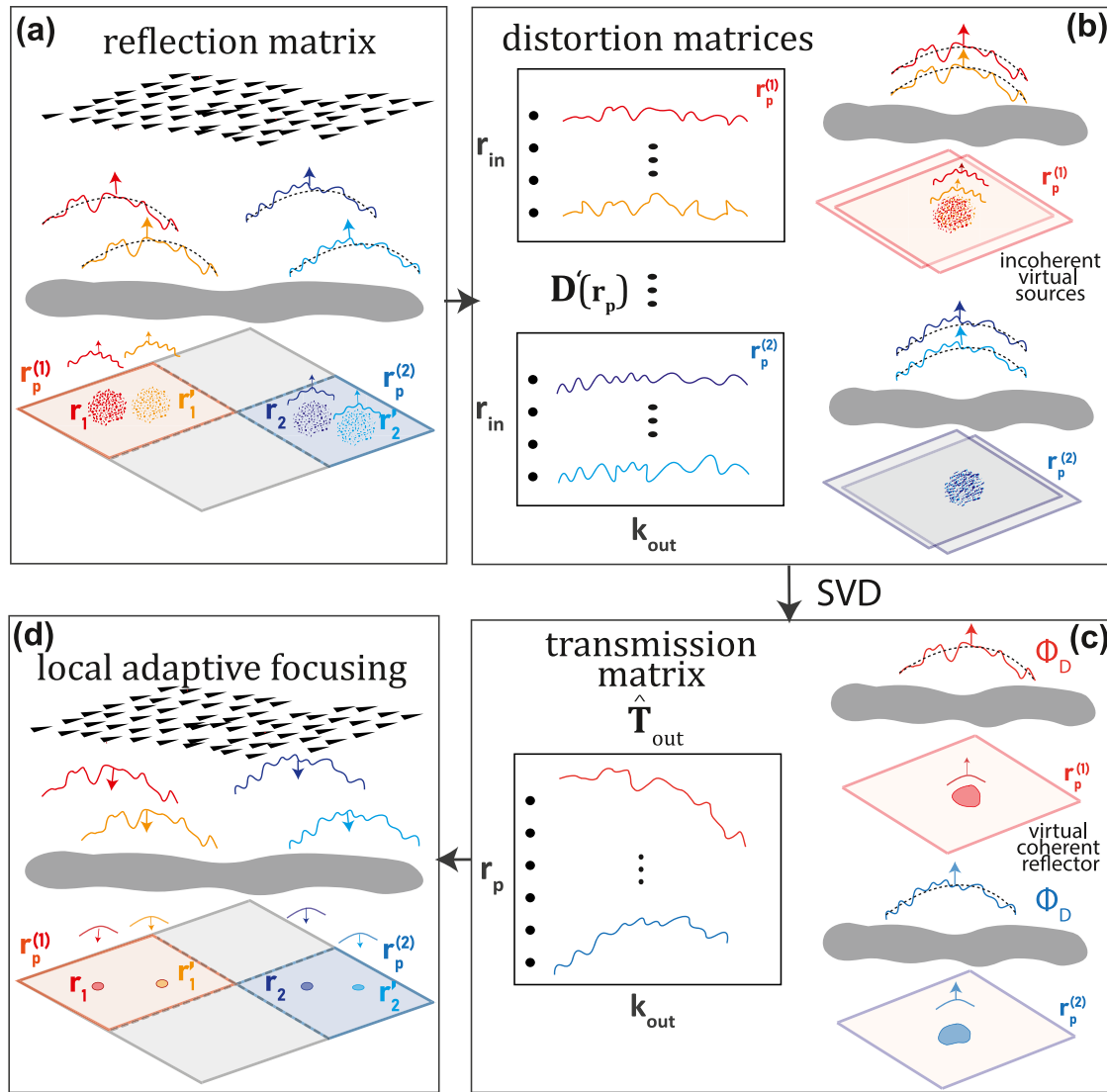


Figure 7. Local aberration correction. (a) One-side plane wave decomposition of each CLASS matrix yields the reflected wave-front associated with each focusing point \mathbf{r}_{in} . (b) By removing the geometrical curvature of each reflected wavefront (dashed line in a), one can study the phase distortions over each isoplanatic patch identified by their midpoint \mathbf{r}_p . This operation amounts to realigning the wavefronts in each isoplanatic area as if they were generated by input focal spots virtually shifted to the origin. (c) SVD of each distortion matrix yields an aberration phase law ϕ_D for each spatial window by combining coherently each focal spot to synthesize a virtual coherent reflector. The set of aberration phase laws forms the estimator $\hat{\mathbf{T}}$ of the transmission matrix. (g) The phase conjugate of $\hat{\mathbf{T}}$ provides the focusing laws to compensate for phase distortions for each patch \mathbf{r}_p .

spatial correlations are highlighted between distorted wave-fields induced by neighbor virtual sources \mathbf{r}_{in} (Badon et al., 2020). Such correlations are a manifestation of a spatial invariance of residual aberrations over areas generally referred to as isoplanatic patches (Lambert, Cobus, et al., 2022).

4.2. Local Distortion Matrices

Our strategy is to divide the field-of-view into a set of overlapping regions (Figure 6d). Each region is defined by a central midpoint $\mathbf{r}_p = (\rho_p, z_p)$ and a spatial extension L . For each region, the local residual \mathbf{D} -matrix is defined as:

$$D'(\mathbf{k}_{out}, \rho_{in}, \mathbf{r}_p) = D(\mathbf{k}_{out}, \rho_{in}, z_p)W(\rho_{in} - \rho_p), \quad (32)$$

where $W(\rho)$ is a spatial window function such that $W(\rho) = 1$ for $|x| < L$ and $|y| < L$, and zero elsewhere. Ideally, wave-front distortions should be invariant over each region, meaning that the virtual sources $\mathbf{r}_{\text{in}} = (\rho_{\text{in}}, z)$ associated with each region belong to the same isoplanatic patch. However, in practice, this hypothesis is not fulfilled. The isoplanatic length actually scales as the typical transverse dimension over which the wave velocity fluctuates. On the one hand, the dimension L of the window function should therefore be reduced to cover the smallest isoplanatic region as possible in order to provide a local and sharp measurement of aberrations. On the other hand, it should also be large enough to include a sufficient number of realizations of disorder in order to unscramble the effect of aberrations from the medium's reflectivity (Lambert, Cobus, et al., 2022). To reach a good estimate of the aberration phase law, the number of input focusing points in each region should be one order of magnitude larger than the number of resolution cells mapping the CLASS focal spot (Figure 6c) (Lambert, Cobus, Frappart, et al., 2020). This is why the initial CLASS step was important to initiate the aberration correction process and reduce the extension of the focal spots before a local and finer compensation of residual aberration by means of the \mathbf{D} -matrix concept. The area covered by the CLASS focal spot being $20 \times 14 \text{ km}^2$ (Figure 6c), the extent of the window is chosen to be $55 \times 55 \text{ km}^2$.

4.3. Singular Value Decomposition

Assuming local isoplanicity in each spatial window W (Equation 17), the coefficients of each distortion matrix $\mathbf{D}'(\mathbf{r}_p)$ matrix can be expressed as follows (Lambert, Cobus, Frappart, et al., 2020):

$$\mathbf{D}'(\mathbf{k}_{\text{out}}, \rho_{\text{in}}, \mathbf{r}_p) = \delta \tilde{\mathbf{H}}_L(\mathbf{k}_{\text{out}}, \mathbf{r}_p) \underbrace{\int d\rho \gamma(\rho + \rho_{\text{in}}, z) \delta H_L(\rho, \mathbf{r}_p) e^{i\mathbf{k}_{\text{out}} \cdot \rho}}_{\text{virtual source}}, \quad (33)$$

This equation can be seen as a product between two terms: the output aberration transmittance and a virtual source term modulated by the medium's fluctuating reflectivity $\gamma(\rho, z)$. The goal is now to unscramble these two terms in order to get a proper estimation of the aberration transmittance $\delta \tilde{\mathbf{H}}_L(\mathbf{k}_{\text{out}}, \mathbf{r}_p)$ at each point \mathbf{r}_p .

In practice, this can be done through a singular value decomposition (SVD) of each local distortion matrix $\mathbf{D}'(\mathbf{r}_p)$:

$$\mathbf{D}'(\mathbf{r}_p) = \mathbf{U}(\mathbf{r}_p) \times \mathbf{\Sigma}(\mathbf{r}_p) \times \mathbf{V}(\mathbf{r}_p)^\dagger \quad (34)$$

where $\mathbf{\Sigma}$ is a diagonal matrix containing the real positive singular values σ_i in a decreasing order $\sigma_1 > \sigma_2 > \dots > \sigma_N$. $\mathbf{U}(\mathbf{r}_p)$ and $\mathbf{V}(\mathbf{r}_p)$ are unitary matrices whose columns, $\mathbf{U}_i(\mathbf{r}_p) = [U_i(\mathbf{k}_{\text{out}}, \mathbf{r}_p)]$ and $\mathbf{V}_i(\mathbf{r}_p) = [V_i(\mathbf{r}_{\text{in}}, \mathbf{r}_p)]$, correspond to the output and input singular vectors, respectively. The physical meaning of this SVD can be intuitively understood by considering the asymptotic case of a point-like input focusing beam: $\delta H_L(\rho, \mathbf{r}_p) = \delta(\rho)$. In this ideal case, Equation 33 becomes: $\mathbf{D}'(\mathbf{k}_{\text{out}}, \rho_{\text{in}}, \mathbf{r}_p) = \delta \tilde{\mathbf{H}}_L(\mathbf{k}_{\text{out}}, \mathbf{r}_p) \gamma(\rho_{\text{in}}, z_p)$. Comparison with Equation 34 shows that, in a first approximation, $\mathbf{D}'(\mathbf{r}_p)$ is of rank 1. The first output singular vector $\mathbf{U}_1(\mathbf{r}_p)$ yields the residual aberration transmittance $\delta \tilde{\mathbf{H}}_L(\mathbf{r}_p)$ while the first input singular vector $\mathbf{V}_1(\mathbf{r}_p)$ directly provides the medium reflectivity over the spatial window W .

However, despite the CLASS correction, the input PSF δH_L remains far from being point-like (Figure 6c). The spectrum of $\mathbf{D}'(\mathbf{r}_p)$ then displays a continuum of singular values but the first eigenstate of $\mathbf{D}'(\mathbf{r}_p)$ is still of interest. $\mathbf{V}_1(\mathbf{r}_p)$ corresponds to a rough estimate of the medium reflectivity that allows realignment in phase for each input focal spot. Therefore, the SVD process allows the synthesis of a coherent virtual reflector that can be leveraged for the estimation of the residual aberration transmittance $\delta \tilde{\mathbf{H}}_L(\mathbf{r}_p)$ (Figure 7c). More precisely, this is the normalized output singular vector $\hat{\mathbf{U}}_1(\mathbf{r}_p) = [U_1(\mathbf{k}_{\text{out}}, \mathbf{r}_p) / |U_1(\mathbf{k}_{\text{out}}, \mathbf{r}_p)|]$, that constitutes a relevant estimator for $\delta \tilde{\mathbf{H}}_L(\mathbf{r}_p)$ (Lambert, Cobus, et al., 2022). The estimator of the transmission matrix is then given by the Hadamard product:

$$\hat{\mathbf{T}}_{\text{out}}(\mathbf{r}_p) = \mathbf{P}'_0 \circ e^{i[\phi_D^{(\text{out})}(\mathbf{r}_p) + \phi_C^{(\text{out})}(z_p)]} \quad (35)$$

with $\phi_D^{(\text{out})}(\mathbf{r}_p)$, the phase of $\hat{\mathbf{U}}_1(\mathbf{r}_p)$. The phase conjugate of $\hat{\mathbf{T}}_{\text{out}}$ provides the focusing laws to compensate for the output phase distortions over each patch (Figure 7d). The same method can be repeated by exchanging the focused and Fourier bases between input and output in order to estimate the transmission matrix \mathbf{T}_{in} (Lambert, Cobus, et al., 2022). The whole process is iterated once to refine the estimation of \mathbf{T}_{out} and \mathbf{T}_{in} .

Table 2
Confocal Gain and Resolution at Each Step of the Aberration Correction Process

Correction steps	0	1	2	3	4	5	6
Correction type	0	CLASS	CLASS	D	D	D	D
Correction side		Output	Input	Output	Input	Output	Input
Confocal gain (dB)		2.41	5.17	7.1	9	9.16	9.26
Resolution w (km)	40	20	8	7	6	6	6

4.4. Transmission Matrix Estimator

The input phase laws obtained at the end of the aberration correction process are displayed in Figure 6e for the central regions of the field-of-view highlighted in Figure 6d. Although they show some similar features (in particular the low spatial frequency components), they also display some differences that are quantified by the correlation coefficient between the different phase masks with the central one. The value of this coefficient is reported below each phase mask. This correlation coefficient goes from 0.86 for the closest spatial windows to 0.39 for the furthest ones. One can also notice that clear differences in the phase behavior can be observed between the north, center and the south of the field-of-view. The presence of these lateral differences is consistent with the three geological blocks in the region (Figure 1b). The latter observation together with the correlation coefficient value show the importance of estimating a different phase law for each area and justifies the implementation of a local aberration correction process.

4.5. Local Compensation of Spatially Distributed Aberrations

Using $\hat{\mathbf{T}}_{\text{out}}$ and $\hat{\mathbf{T}}_{\text{in}}$, a corrected FR matrix can be finally obtained:

$$\mathbf{R}_{\rho\rho}^{(D)}(z) = \hat{\mathbf{T}}_{\text{out}}^{\dagger}(z) \times \mathbf{R}_{\text{kk}}(z) \times \hat{\mathbf{T}}_{\text{in}}^*(z) \quad (36)$$

The corresponding confocal image and RPSF are displayed at $z = 25$ km in Figures 6d and 6f. The comparison with their CLASS counterparts (Figures 6a and 6c) shows the importance of the local \mathbf{D} – matrix analysis. The diffuse background is clearly reduced and the RPSF is nearly similar to its ideal value (Figure 3d), with almost all the backscattered energy contained in the white circle accounting for the diffraction limit. The residual background in Figure 6f is probably associated with high-order aberrations whose coherence length (isoplanatic area) is smaller than the size L of the window function $W(\rho)$.

To be more quantitative, a confocal gain can be computed from the intensity ratio between the corrected (Figures 6a and 6d) and initial (Figure 3e) images. The transverse resolution can also be estimated from the full width at half maximum w of the RPSF. The confocal gain and the resolution are reported in Table 2 at each step of the aberration correction process for depth $z = 25$ km. Strikingly, the transverse resolution is enhanced by a factor ~ 7 compared with its initial value and the confocal intensity is increased by more than 9 dB. These values highlight the benefit of matrix imaging for in-depth probing of NAFZ at a large scale.

In the next section, the 3D image of the medium around the NAFZ is now revealed by combining the images derived at each depth. A structural interpretation is then provided in light of previous studies on the NAFZ.

5. 3D Structure of the NAFZ

The previous sections have shown the process for a local compensation of phase distortions. Performing this correction process at each depth allows to uncover a well-resolved 3D image of the subsurface.

Figure 8a shows a North-South cross-section from the final 3D image. This cross-section is chosen at the same location as the one in Figure 4a and crosses the two fault strands. It also spans the three geological units: Istanbul zone (IZ), Armutlu-Almacik (AA) and Sakarya zone (SZ). The scattering generated by the heterogeneities of the medium induce a decrease of the backscattered energy with depth. Consequently, a drop of amplitude is observed in the 3D images. In order to compensate for this, the intensity in the cross-sections is normalized by the mean intensity calculated at each depth.

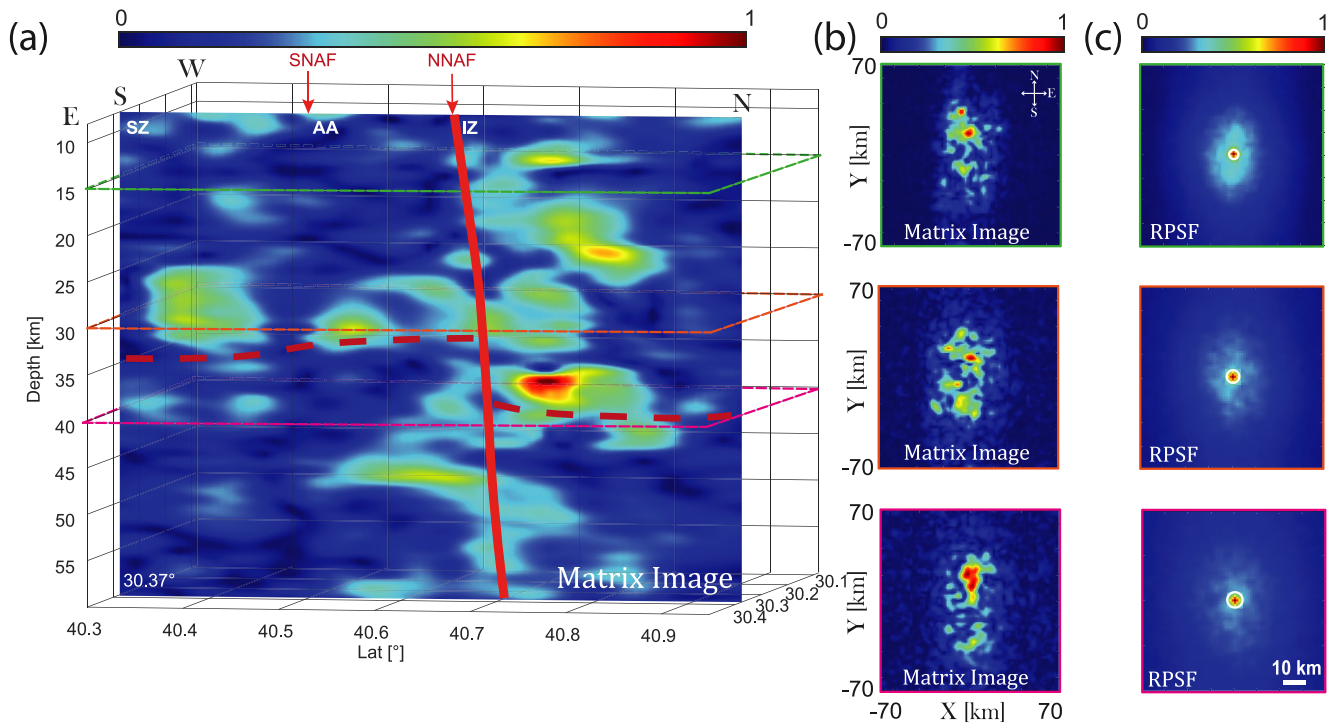


Figure 8. Final image of North Anatolian Fault zone. (a) Vertical North-South cross-section at 30.37°E . The North-South profile is oriented perpendicular to the fault traces. The location of the profile is shown in Figure 1a. The locations of the southern (SNAF) and northern (NNAF), and the major crustal blocks (SZ: Sakarya zone, AA: Armutlu-Almacik and IZ: Istanbul zone) are labeled. The interpreted location of the fault at depth are indicated by a red line. The color scale refers to the scattering intensity. It is normalized by the maximum value of the scattering energy inside the volume. Our interpretation of the Moho's location is indicated by red dashed lines. (b) Depth slices retrieved from the 3D scattering volume at $z = 15, 30$ and 40 km with (c) their corresponding RPSFs.

Three depth slices retrieved from the final 3D images at $z = 15, 30$ and 40 km are also represented in Figure 8b with their corresponding RPSFs in Figure 8c. Compared to the initial RPSFs (Figure 4c), the resolution is significantly improved by a factor that increases from 7 at small depth ($z < 15$ km) to 9 beyond $z = 40$ km. The final matrix images in Figure 8b can also be compared to the initial confocal ones in Figure 4b. While the original images show random-like features, the images obtained after aberration correction reveal better defined features and a reflectivity that is mainly concentrated in the North. The same observation can be made by looking at the corrected cross-section in Figure 8a. The differences between the corrected and raw cross-sections are pronounced. While in the raw image, no clear structures and layers are visible, the corrected image reveals sub-horizontal structures with a refined level of details, thanks to the drastic gain in resolution revealed by the RPSF.

Due to its significant seismic activity over the past 100 years, and to assess the ongoing hazard posed by this activity, extensive research has been conducted on the NAFZ to image its structure and determine its mechanical characteristics. The scattering structure in Figure 8a is interpreted with reference to prior studies conducted in the region.

The first thing to notice in the profiles is that the scattered energy is predominantly situated in the North, which corresponds with the location of the Northern branch. This observation may be associated with the greater seismic activity of the Northern strand compared to the seismic activity of the Southern strand. The scattering below this strand and to the North of it, that extends to at least 60 km, can be explained by the damage caused by the large deformation of this complex fault system with a cumulative slip of the order of 80 km (Armijo et al., 1999; Bohnhoff et al., 2016) during the last million years as well as the heterogeneities that have been inherited from the complex tectonic history of the region.

At the east of the Sea of Marmara, the Moho depth was reported to be between 30 and 35 km (Vanacore et al., 2013; Zor et al., 2003). A deepening of the Moho was identified (~ 40 km) in the IZ by Frederiksen et al. (2015), Taylor et al. (2016), Papaleo et al. (2017, 2018), Rost et al. (2021), and Jenkins et al. (2020). In

Figure 8a, a high scattering zone is observed between 25 and 40 km depth corresponding to a heterogeneous lower crust. Its lower boundary indicates the presence of the Moho (red dashed line). The Moho depth varies from 35 km in the South to 42 km in the North. The reflectivity is disrupted around 40.75°N suggesting the presence of a step in the Moho below the Northern strand. The latter observation is in agreement with previous studies (Jenkins et al., 2020; Rost et al., 2021). Below the Moho, reflective structures are observed, mainly beneath AA and IZ, in agreement with Kahraman et al. (2015). These findings, supported with other studies (Jenkins et al., 2020; Kahraman et al., 2015; Papaleo et al., 2018; Rost et al., 2021), suggest that the NNAF cuts through the entire crust and reaches the upper mantle (Jenkins et al., 2020; Kahraman et al., 2015; Papaleo et al., 2018; Rost et al., 2021). A signature of the NAFZ in the mantle has also been proposed by the long period analysis of Fichtner et al. (2013).

The signature of the Northern strand at depth can be identified by the presence of discontinuities in the scattering distribution in the first 20 km of the crust (Figure 8a) and also by the termination of sub-Moho structures below the Northern strand. The Southern strand, on the other hand, lacks significant scattering, indicating that it has a weaker signal compared to the Northern strand. This, along with the continuity of the Moho in the South, suggests that the SNAF is confined in the crust and does not extend to the upper mantle, Armutlu block being a crustal structure.

In this section, only one cross-section has been depicted to demonstrate the significant enhancements and the gain in resolution provided by the presented matrix approach. A more in-depth analysis of the scattering volume around the NAFZ will be provided in a future study.

6. Conclusion

Matrix imaging provides unprecedented view of the NAFZ. To that aim, we exploited seismic noise data from a dense deployment over the rupture region of the 1999 Izmit earthquake. Ambient noise cross-correlations enable the passive measurement of the reflection matrix associated with the dense array of geophones. The body wave component is then used to image the in-depth reflectivity of the NAFZ subsurface. Compared with our previous work that considered a sparse scattering medium (Touma et al., 2021), the NAFZ case is more general since it exhibits both specular reflectors such as Moho discontinuity and a random distribution of heterogeneities.

The strength of matrix imaging lies in the fact that it does not require an accurate velocity model. Here, a layered velocity model is employed but strong phase distortions subsist since lateral variations of the wave velocity are not taken into account. Nevertheless, such complex aberrations are compensated by two matrix methods previously developed in optical microscopy (Kang et al., 2017; Najar et al., 2023; Yoon et al., 2020) and ultrasound imaging (Bureau et al., 2023; Lambert, Cobus, Frappart, et al., 2020; Lambert, Cobus, Robin, et al., 2022). First, the CLASS algorithm exploits angular correlations and memory effect exhibited by the reflection matrix to compensate for spatially invariant aberrations. Second, a local analysis of the distortion matrix enables a local compensation of spatially distributed aberrations. Together, those two approaches provide a sharp estimate of the transmission matrix between the Earth surface and the subsurface, leading to a narrowing of the imaging PSF by a factor that goes from 7 to 9. Therefore, a diffraction-limited resolution is reached for any pixel of the image.

Thanks to matrix imaging, the scattering structure of the crust and upper mantle of the NAFZ continental strike slip fault is thus revealed. The 60 km depth profile, show terminations of crustal discontinuities mainly below the northern branch. The localized scattering around the NNAF is consistent with the fact that it is the most seismically active fault and that it ruptured during the last 7.6 Izmit earthquake. We identify a step in the Moho coinciding with the surface location of this branch in the East of DANA network. Moreover, the scattering extends to the upper mantle in the North. All these observations are consistent with previous studies and suggest that the NNAFZ is localized in the crust and extends to the upper mantle.

Even though the result are promising, several points remain that would allow improved images. First, potential conversion between S and P-waves is not considered by matrix imaging. The method could be improved in the future by considering both longitudinal and shear waves, as well as wave conversion between them. Second, only a broadband compensation of phase distortions is performed. Yet, scattering phenomena or multiple reflections would require a procedure that moves beyond the application of simple time delays to the impulse response between geophones. Finally, a reflectivity image is only qualitative since it does not directly quantify the mechanical properties of the subsurface. Yet matrix imaging offers the possibility of mapping the velocity distribution inside the medium (Lambert, Cobus, Couade, et al., 2020). This will be the focus of a future study.

Data Availability Statement

The data used for this study were recorded by the temporary Dense Array for North Anatolia (DANA) and can be found at (DANA, 2012). The cross-correlation data and codes used to post-process the seismic data within this paper have been deposited at (Touma et al., 2023).

Acknowledgments

This project has received funding from the European Research Council (ERC) under the European Union Horizon 2020 research and innovation program (grant agreement No 742335, F-IM-AGE and grant agreement No. 819261, REMINISCENCE).

References

- Akbarbayram, K., Sorlien, C. C., & Okay, A. I. (2016). Evidence for a minimum 52±1 km of total offset along the northern branch of the North Anatolian Fault in northwest Turkey. *Tectonophysics*, 668, 35–41. <https://doi.org/10.1016/j.tecto.2015.11.026>
- Akyuz, H., Hartleb, R., Barka, A., Altunel, E., Sunal, G., Meyer, B., & Armijo, V. R. (2002). Surface rupture and slip distribution of the 12 November 1999 Duzce earthquake (m 7.1), North Anatolian fault, Bolu, Turkey. *Bulletin of the Seismological Society of America*, 92(1), 61–66. <https://doi.org/10.1785/0120000840>
- Ambraseys, N. (2002). Seismic sea-waves in the Marmara Sea region during the last 20 centuries. *Journal of Seismology*, 6(4), 571–578. <https://doi.org/10.1023/a:1021158610252>
- Ambraseys, N. N., & Finkel, C. (1995). *The seismicity of Turkey and adjacent areas: A historical review* (pp. 1500–1800). MS Eren.
- Armijo, R., Meyer, B., Hubert, A., & Barka, A. (1999). Westward propagation of the North Anatolian Fault into the Northern Aegean: Timing and kinematics. *Geology*, 27(3), 267–270. [https://doi.org/10.1130/0091-7613\(1999\)027<0267:wpotna>2.3.co;2](https://doi.org/10.1130/0091-7613(1999)027<0267:wpotna>2.3.co;2)
- Aubry, A., & Derode, A. (2009). Detection and imaging in a random medium: A matrix method to overcome multiple scattering and aberration. *Journal of Applied Physics*, 106(4). <https://doi.org/10.1063/1.3200962>
- Badon, A., Barolle, V., Irsch, K., Boccara, A. C., Fink, M., & Aubry, A. (2020). Distortion matrix concept for deep imaging in optical coherence microscopy. *Science Advances*, 6, eaay7170.
- Barka, A. (1992). The North Anatolian fault zone. In *Annales tectonicae* (Vol. 6, pp. 164–195).
- Barka, A., Akyuz, H., Altunel, E., Sunal, G., Cakir, Z., Dikbas, A., et al. (2002). The surface rupture and slip distribution of the 17 august 1999 Izmit earthquake (M 7.4), North Anatolian fault. *Bulletin of the Seismological Society of America*, 92(1), 43–60. <https://doi.org/10.1785/0120000841>
- Bensen, G., Ritzwoller, M., Barmin, M., Levshin, A. L., Lin, F., Moschetti, M., et al. (2007). Processing seismic ambient noise data to obtain reliable broad-band surface wave dispersion measurements. *Geophysical Journal International*, 169(3), 1239–1260. <https://doi.org/10.1111/j.1365-246x.2007.03374.x>
- Berkhout, A. (1981). Wave field extrapolation techniques in seismic migration, a tutorial. *Geophysics*, 46(12), 1638–1656. <https://doi.org/10.1190/1.1441172>
- Berkhout, A. J., & Wapenaar, C. P. A. (1993). A unified approach to acoustical reflection imaging. II: The inverse problem. *Journal of the Acoustical Society of America*, 93(4), 2017–2023. <https://doi.org/10.1121/1.406715>
- Blondel, T., Chaput, J., Derode, A., Campillo, M., & Aubry, A. (2018). Matrix approach of seismic imaging: Application to the Erebus volcano, Antarctica. *Journal of Geophysical Research: Solid Earth*, 123(12), 10936–10950. <https://doi.org/10.1029/2018jb016361>
- Bohnhoff, M., Martínez-Garzón, P., Bulut, F., Stierle, E., & Ben-Zion, Y. (2016). Maximum earthquake magnitudes along different sections of the North Anatolian fault zone. *Tectonophysics*, 674, 147–165. <https://doi.org/10.1016/j.tecto.2016.02.028>
- Born, M., & Wolf, E. (2003). *Principles of optics* (7th ed.). Cambridge University Press.
- Bureau, F., Robin, J., Le Ber, A., Lambert, W., Fink, M., & Aubry, A. (2023). Three-dimensional ultrasound matrix imaging. *Nature Communications*, 14(1), 6793. <https://doi.org/10.1038/s41467-023-42338-8>
- Campillo, M., & Paul, A. (2003). Long-range correlations in the diffuse seismic coda. *Science*, 299(5606), 547–549. <https://doi.org/10.1126/science.1078551>
- Campillo, M., & Roux, P. (2014). Seismic imaging and monitoring with ambient noise correlations. *Treatise on Geophysics*, 1, 256–271.
- Chen, F., Siebel, W., Satir, M., Terzioğlu, M., & Saka, K. (2002). Geochronology of the Karadere basement (NW Turkey) and implications for the geological evolution of the Istanbul zone. *International Journal of Earth Sciences*, 91(3), 469–481. <https://doi.org/10.1007/s00531-001-0239-6>
- Choi, C., Song, K.-D., Kang, S., Park, J.-S., & Choi, W. (2018). Optical imaging featuring both long working distance and high spatial resolution by correcting the aberration of a large aperture lens. *Scientific Reports*, 8(1), 1–12. <https://doi.org/10.1038/s41598-018-27289-1>
- Çubuk-Sabuncu, Y., Taymaz, T., & Fichtner, A. (2017). 3-D crustal velocity structure of western Turkey: Constraints from full-waveform tomography. *Physics of the Earth and Planetary Interiors*, 270, 90–112. <https://doi.org/10.1016/j.pepi.2017.06.014>
- DANA (2012). Dense array for North Anatolia (DANA) [Online Dataset]. International Federation of Digital Seismograph Networks. https://doi.org/10.7914/SN/YH_2012
- Draganov, D., Wapenaar, K., Mulder, W., Singer, J., & Verdel, A. (2007). Retrieval of reflections from seismic background-noise measurements. *Geophysical Research Letters*, 34(4), L04305. <https://doi.org/10.1029/2006gl028735>
- Emre, Ö., Duman, T. Y., Özalp, S., Şaroğlu, F., Olgun, Ş., Elmacı, H., & Çan, T. (2018). Active fault database of Turkey. *Bulletin of Earthquake Engineering*, 16(8), 3229–3275. <https://doi.org/10.1007/s10518-016-0041-2>
- Fichtner, A., Saygin, E., Taymaz, T., Cupillard, P., Capdeville, Y., & Trampert, J. (2013). The deep structure of the North Anatolian fault zone. *Earth and Planetary Science Letters*, 373, 109–117. <https://doi.org/10.1016/j.epsl.2013.04.027>
- Frederiksen, A., Thompson, D., Rost, S., Cornwell, D., Gülen, L., Houseman, G., et al. (2015). Crustal thickness variations and isostatic disequilibrium across the North Anatolian Fault, western Turkey. *Geophysical Research Letters*, 42(3), 751–757. <https://doi.org/10.1002/2014gl02401>
- Freund, I., Rosenbluh, M., & Feng, S. (1988). Memory effects in propagation of optical waves through disordered media. *Physical Review Letters*, 61(20), 2328–2331. <https://doi.org/10.1103/physrevlett.61.2328>
- Giraudat, E., Burtin, A., & Aubry, A. (2021). Passive seismic matrix imaging of La Soufrière de Guadeloupe volcano. In *EGU general assembly conference abstracts*.
- Hasselmann, K. (1963). A statistical analysis of the generation of microseisms. *Reviews of Geophysics*, 1(2), 177–210. <https://doi.org/10.1029/rg001i002p00177>
- Jenkins, J., Stephenson, S. N., Martínez-Garzón, P., Bohnhoff, M., & Nurlu, M. (2020). Crustal thickness variation across the Sea of Marmara region, NW Turkey: A reflection of modern and ancient tectonic processes. *Tectonics*, 39(7), e2019TC005986. <https://doi.org/10.1029/2019tc005986>
- Kahraman, M., Cornwell, D. G., Thompson, D. A., Rost, S., Houseman, G. A., Türkelli, N., et al. (2015). Crustal-scale shear zones and heterogeneous structure beneath the north Anatolian Fault Zone, Turkey, revealed by a high-density seismometer array. *Earth and Planetary Science Letters*, 430, 129–139. <https://doi.org/10.1016/j.epsl.2015.08.014>

- Kang, S., Jeong, S., Choi, H., Ko, W., Yang, T. D., Joo, J. H., et al. (2015). Imaging deep within a scattering medium using collective accumulation of single-scattered waves. *Nature Photonics*, 9(4), 1–18. <https://doi.org/10.1038/nphoton.2015.24>
- Kang, S., Kang, P., Jeong, S., Kwon, Y., Yang, T. D., Hong, J. H., et al. (2017). High-resolution adaptive optical imaging within thick scattering media using closed-loop accumulation of single scattering. *Nature Communications*, 8(1), 1–10. <https://doi.org/10.1038/s41467-017-02117-8>
- Karahan, A. E., Berckheimer, H., & Baier, B. (2001). Crustal structure at the western end of the North Anatolian Fault Zone from deep seismic sounding. *Annales Geophysicae*, 44.
- Koulakov, I., Bindi, D., Parolai, S., Grosser, H., & Milkereit, C. (2010). Distribution of seismic velocities and attenuation in the crust beneath the North Anatolian Fault (Turkey) from local earthquake tomography. *Bulletin of the Seismological Society of America*, 100(1), 207–224. <https://doi.org/10.1785/0120090105>
- Lambert, W., Cobus, L. A., Couade, M., Fink, M., & Aubry, A. (2020). Reflection matrix approach for quantitative imaging of scattering media. *Physical Review X*, 10(2), 021048. <https://doi.org/10.1103/physrevx.10.021048>
- Lambert, W., Cobus, L. A., Frappart, T., Fink, M., & Aubry, A. (2020). Distortion matrix approach for ultrasound imaging of random scattering media. *Proceedings of the National Academy of Sciences of the United States of America*, 117(26), 14645–14656. <https://doi.org/10.1073/pnas.1921533117>
- Lambert, W., Cobus, L. A., Robin, J., Fink, M., & Aubry, A. (2022). Ultrasound matrix imaging—Part II: The distortion matrix for aberration correction over multiple isoplanatic patches. *IEEE Transactions on Medical Imaging*, 41(12), 3921–3938. <https://doi.org/10.1109/tmi.2022.3199483>
- Lambert, W., Robin, J., Cobus, L. A., Fink, M., & Aubry, A. (2022). Ultrasound matrix imaging—Part I: The focused reflection matrix, the F-factor and the role of multiple scattering. *IEEE Transactions on Medical Imaging*, 41(12), 3907–3920. <https://doi.org/10.1109/tmi.2022.3199498>
- Longuet-Higgins, M. S. (1950). A theory of the origin of microseisms. *Philosophical Transactions of the Royal Society A*, 243(857), 1–35.
- Lyakhovskiy, V., & Ben-Zion, Y. (2009). Evolving geometrical and material properties of fault zones in a damage rheology model. *Geochemistry, Geophysics, Geosystems*, 10(11), Q11011. <https://doi.org/10.1029/2009gc002543>
- Najar, U., Barolle, V., Balondrade, P., Fink, M., Boccara, A. C., Fink, M., & Aubry, A. (2023). Non-invasive retrieval of the time-gated transmission matrix for optical imaging deep inside a multiple scattering medium. arXiv: 2303.06119.
- Okay, A. I., & Tüysüz, O. (1999). Tethyan sutures of northern Turkey. *Geological Society, London, Special Publications*, 156(1), 475–515. <https://doi.org/10.1144/gsl.sp.1999.156.01.22>
- Papaleo, E., Cornwell, D., & Rawlinson, N. (2018). Constraints on North Anatolian Fault Zone width in the crust and upper mantle from S wave teleseismic tomography. *Journal of Geophysical Research: Solid Earth*, 123(4), 2908–2922. <https://doi.org/10.1002/2017jb015386>
- Papaleo, E., Cornwell, D. G., & Rawlinson, N. (2017). Seismic tomography of the North Anatolian Fault: New insights into structural heterogeneity along a continental strike-slip fault. *Geophysical Research Letters*, 44(5), 2186–2193. <https://doi.org/10.1002/2017gl072726>
- Poli, P., Campillo, M., Pedersen, H., & LAPNET Working Group. (2012). Body-wave imaging of Earth's mantle discontinuities from ambient seismic noise. *Science*, 338(6110), 1063–1065. <https://doi.org/10.1126/science.1228194>
- Poli, P., Pedersen, H., & Campillo, M. (2012). Emergence of body waves from cross-correlation of short period seismic noise. *Geophysical Journal International*, 188(2), 549–558. <https://doi.org/10.1111/j.1365-246x.2011.05271.x>
- Qian, R., & Liu, L. (2020). Imaging the active faults with ambient noise passive seismics and its application to characterize the Huangzhuang-Gaoliying fault in Beijing Area, northern China. *Engineering Geology*, 268, 105520. <https://doi.org/10.1016/j.enggeo.2020.105520>
- Reilinger, R., McClusky, S., Vernant, P., Lawrence, S., Ergintav, S., Cakmak, R., et al. (2006). Gps constraints on continental deformation in the Africa-Arabia-Eurasia continental collision zone and implications for the dynamics of plate interactions. *Journal of Geophysical Research: Solid Earth*, 111(B5), B05411. <https://doi.org/10.1029/2005jb004051>
- Retailleau, L., Boué, P., Li, L., & Campillo, M. (2020). Ambient seismic noise imaging of the lowermost mantle beneath the North Atlantic Ocean. *Geophysical Journal International*, 222(2), 1339–1351. <https://doi.org/10.1093/gji/ggaa210>
- Rost, S., Houseman, G., Frederiksen, A., Cornwell, D., Kahraman, M., Altuncu Poyraz, S., et al. (2021). Structure of the northwestern North Anatolian Fault Zone imaged via teleseismic scattering tomography. *Geophysical Journal International*, 227(2), 922–940. <https://doi.org/10.1093/gji/ggab265>
- Salah, M. K., Sahin, S., & Kaplan, M. (2007). *Seismic velocity structure along the western segment of the North Anatolian fault zone imaged by seismic tomography* (Vol. 82, pp. 209–223). Bulletin of the Earthquake Research Institute, University of Tokyo.
- Sengör, A. (1979). The North Anatolian transform fault: Its age, offset and tectonic significance. *Journal of the Geological Society of London*, 136(3), 269–282. <https://doi.org/10.1144/gsjgs.136.3.0269>
- Shahjahan, S., Aubry, A., Rupin, F., Chassignole, B., & Derode, A. (2014). A random matrix approach to detect defects in a strongly scattering polycrystal: How the memory effect can help overcome multiple scattering. *Applied Physics Letters*, 104(23). <https://doi.org/10.1063/1.4882421>
- Shapiro, N. M., & Campillo, M. (2004). Emergence of broadband Rayleigh waves from correlations of the ambient seismic noise. *Geophysical Research Letters*, 31(7), L07614. <https://doi.org/10.1029/2004gl019491>
- Stehly, L., Campillo, M., & Shapiro, N. (2006). A study of the seismic noise from its long-range correlation properties. *Journal of Geophysical Research: Solid Earth*, 111(B10), B10306. <https://doi.org/10.1029/2005jb004237>
- Stein, R. S., Barka, A. A., & Dieterich, J. H. (1997). Progressive failure on the North Anatolian fault since 1939 by earthquake stress triggering. *Geophysical Journal International*, 128(3), 594–604. <https://doi.org/10.1111/j.1365-246x.1997.tb05321.x>
- Taylor, G., Rost, S., & Houseman, G. (2016). Crustal imaging across the North Anatolian Fault Zone from the autocorrelation of ambient seismic noise. *Geophysical Research Letters*, 43(6), 2502–2509. <https://doi.org/10.1002/2016gl067715>
- Taylor, G., Rost, S., Houseman, G. A., & Hillers, G. (2019). Near-surface structure of the North Anatolian Fault zone from Rayleigh and Love wave tomography using ambient seismic noise. *Solid Earth*, 10(2), 363–378. <https://doi.org/10.5194/se-10-363-2019>
- Touma, R., Blondel, T., Derode, A., Campillo, M., & Aubry, A. (2021). A distortion matrix framework for high-resolution passive seismic 3-D imaging: Application to the San Jacinto fault zone, California. *Geophysical Journal International*, 226(2), 780–794. <https://doi.org/10.1093/gji/ggab133>
- Touma, R., Le Ber, A., Campillo, M., & Aubry, A. (2023). Seismic matrix imaging [Software]. Figshare. <https://doi.org/10.6084/m9.figshare.23802630>
- Vanacore, E., Taymaz, T., & Saygin, E. (2013). Moho structure of the Anatolian Plate from receiver function analysis. *Geophysical Journal International*, 193(1), 329–337. <https://doi.org/10.1093/gji/ggs107>
- Vauchez, A., Tommasi, A., & Mainprice, D. (2012). Faults (shear zones) in the Earth's mantle. *Tectonophysics*, 558, 1–27. <https://doi.org/10.1016/j.tecto.2012.06.006>
- Yılmaz, Y., Genç, Ş., Yiğitbaş, E., Bozcu, M., & Yılmaz, K. (1995). Geological evolution of the late Mesozoic continental margin of Northwest Anatolia. *Tectonophysics*, 243(1–2), 155–171. [https://doi.org/10.1016/0040-1951\(94\)00196-g](https://doi.org/10.1016/0040-1951(94)00196-g)

- Yoon, S., Lee, H., Hong, J. H., Lim, Y.-S., & Choi, W. (2020). Laser scanning reflection-matrix microscopy for aberration-free imaging through intact mouse skull. *Nature Communications*, *11*(1), 5721. <https://doi.org/10.1038/s41467-020-19550-x>
- Zigone, D., Ben-Zion, Y., Lehujeur, M., Campillo, M., Hillers, G., & Vernon, F. L. (2019). Imaging subsurface structures in the San Jacinto fault zone with high-frequency noise recorded by dense linear arrays. *Geophysical Journal International*, *217*(2), 879–893. <https://doi.org/10.1093/gji/ggz069>
- Zor, E., Sandvol, E., Gürbüz, C., Türkelli, N., Seber, D., & Barazangi, M. (2003). The crustal structure of the East Anatolian plateau (Turkey) from receiver functions. *Geophysical Research Letters*, *30*(24), 8044. <https://doi.org/10.1029/2003gl018192>